Opto-Electronic Advances

ISSN 2096-4579 CN 51-1781/TN

Liquid crystal-integrated metasurfaces for an active photonic platform

Dohyun Kang, Hyeonsu Heo, Younghwan Yang, Junhwa Seong, Hongyoon Kim, Joohoon Kim and Junsuk Rho

Citation: Kang DH, Heo HS, Yang YH, et al. Liquid crystal-integrated metasurfaces for an active photonic platform. *Opto-Electron Adv* **7**, 230216(2024).

https://doi.org/10.29026/oea.2024.230216

Received: 1 December 2023; Accepted: 19 January 2024; Published online: 25 April 2024

Opto-Electronic Advances

Review

June 2024, Vol. 7, No. 6

DOI: 10.29026/oea.2024.230216

Liquid crystal-integrated metasurfaces for an active photonic platform

Dohyun Kang[1†], Hyeonsu Heo[1†], Younghwan Yang[1†], Junhwa Seong[1], Hongyoon Kim[1], Joohoon Kim[1] and Junsuk Rho[1,2,3,4,5*]

Metasurfaces have opened the door to next-generation optical devices due to their ability to dramatically modulate electromagnetic waves at will using periodically arranged nanostructures. However, metasurfaces typically have static optical responses with fixed geometries of nanostructures, which poses challenges for implementing transition to technology by replacing conventional optical components. To solve this problem, liquid crystals (LCs) have been actively employed for designing tunable metasurfaces using their adjustable birefringent in real time. Here, we review recent studies on LC-powered tunable metasurfaces, which are categorized as wavefront tuning and spectral tuning. Compared to numerous reviews on tunable metasurfaces, this review intensively explores recent development of LC-integrated metasurfaces. At the end of this review, we briefly introduce the latest research trends on LC-powered metasurfaces and suggest further directions for improving LCs. We hope that this review will accelerate the development of new and innovative LC-powered devices.

Keywords: tunable metasurface; liquid crystal; active metasurface; electrically tunable optical system

Kang DH, Heo HS, Yang YH et al. Liquid crystal-integrated metasurfaces for an active photonic platform. *Opto-Electron Adv* **7**, 230216 (2024).

Introduction

Metasurfaces, which consist of artificially arranged subwavelength structures, also called meta-atoms, have been actively researched due to their planar nature to dramatically modulate electromagnetic waves[1–3]. Numerous applications have been demonstrated with various design approaches for realizing holography[4–11], lensing[12–17], color generation[18–22], and beam-steering[23–26]. Several design methods have been demonstrated: the geometry of meta-atoms, resonance effects, and free-form optimization. The first involves rotating meta-atoms (called Pancharatnam-Berry (PB) phase)[27,28] or changing the parameters such as height, width, and length of meta-atoms (propagation phase). In addition, both PB phase and propagation phase can be used to compensate for each other's disadvantages, with PB phase operating only for circular polarization while propagation phase operates only for orthogonal and linear polarization (LP)[29,30]. The second method involves resonance effects, such as Mie resonance[31–33], Fabry–Pérot (FP) resonance[34–36],

[1]Department of Mechanical Engineering, Pohang University of Science and Technology (POSTECH), Pohang 37673, Republic of Korea; [2]Department of Chemical Engineering, Pohang University of Science and Technology (POSTECH), Pohang 37673, Republic of Korea; [3]Department of Electrical Engineering, Pohang University of Science and Technology (POSTECH), Pohang 36763, Republic of Korea; [4]POSCO-POSTECH-RIST Convergence Research Center for Flat Optics and Metaphotonics, Pohang 37673, Republic of Korea; [5]National Institute of Nanomaterials Technology (NINT), Pohang 37673, Republic of Korea.

[†]These authors contributed equally to this work.

*Correspondence: J Rho, E-mail: jsrho@postech.ac.kr

Received: 1 December 2023; Accepted: 19 January 2024; Published online: 25 April 2024

guided-mode resonance (GMR)[37,38], and bound states in the continuum (BIC) resonance[39–41]. Finally, various simulation tools, such as rigorous-coupled wave analysis (RCWA)[42,43], finite-difference time-domain (FDTD)[44–46], and finite element methods (FEM)[47,48] can be used to optimize meta-atoms. Over the last two decades, these design methods have been employed to potentially replace conventional optical systems due to their standout features such as high numerical aperture (NA) and wide field of view (FOV).

However, their passive nature — having one specific function once fabricated — poses a critical problem for broad applications. The tunability of metasurfaces enables their utilization in optical communications or high-resolution sensors. Furthermore, by arranging tunable metasurfaces as a pixelated array, metahologram can be applied for 3D holographic displays, and beam-steering can be implemented for a light detection and ranging (LiDAR) system. These applications strongly support that research on tunable metasurfaces is essential not only for the scientific advancement of metasurfaces but also for their commercial development as a technology.

Tunable metasurfaces can be designed using two main strategies: 1) mechanical tuning based on various external stimuli and 2) combination with active materials. Mechanical tuning involves altering the electromagnetic response by modifying structural aspects, such as adjusting lattice constants, resonator shapes, or spatial arrangements. This is achieved by manipulating the interplay between electromagnetic and elastic forces in response to external stimuli, including thermal input[49–51], electrical input[52–54], and physical tension[55–57]. Combination with active materials involves surrounding media or inserting materials whose optical properties are sensitive to external stimuli, resulting in the dynamic control of metamaterials. Active materials include liquid crystal (LC)[23,58], graphene[59,60], ultrathin metal[61,62], semiconductor[63,64], and superconductor[65,66]. Generally, mechanical tuning methods tend to result in a wider spectrum tuning range, but they exhibit relatively slower response times compared to methods involving active materials[67,68]. In contrast, methods involving active materials offer faster response times but yield narrower spectra.

In this review, we focused on LCs to achieve metasurface tunability due to their exceptional characteristics including birefringence, real-time responsiveness across the visible, infrared (IR), and terahertz (THz) bands, and high transparency in the visible spectrum. Specifically, they can be modulated by various stimuli within a few milliseconds[69], a crucial factor for practical applications. Notably, their demonstrated productivity, exemplified by LC displays (LCDs), showcases their cost-effectiveness and suitability for large-scale production. Furthermore, LCs are among the most widely utilized methods for creating electrically tunable metasurfaces. For instance, graphene exhibits an incredibly fast response time in the picosecond scale; however, its critical weakness lies in its narrow operational spectrum, restricting its functionality in the visible region, thus limiting its practical applications[70,71]. Phase change materials offer reversibility, enabling free switching, but their low energy efficiency poses a challenge for photonic applications[72,73]. MEMS/NEMS, while promising, suffer from high fabrication difficulty and cost, rendering them less viable[68,74]. In contrast, LCs demonstrate mass production stability, boasting high modulation accuracy and reversibility. Consequently, LC-based metasurfaces hold significant potential for practical applications [Table 1]. Despite these advantages, there exists no review paper solely dedicated to LC-powered metasurfaces, unlike the reviews available for various methods in tunable metasurfaces[75–80].

Here, we focus on LC-powered tunable metasurfaces and their potential to expand the practical usability of metasurfaces. Initially, we provide a brief overview of the characteristics of various types of LCs and their alignment technologies. Subsequently, we categorize metasurface-based photonic modulation into wavefront tuning

Table 1 | Comparison of electrical tuning techniques for tunable metasurfaces.

Methods	Response time	Advantages	Disadvantages	Ref.
LC	Millisecond scale	Proven stability for mass production High efficiency	Bulky system	ref.[81,82]
Graphene	Picosecond scale	Fast response time Robust stability	Power consumption Narrow spectrum (NIR to THz)	ref.[70,71]
Phase change materials	Millisecond scale	Reversible	Low energy efficiency	ref.[72,73]
MEMS/NEMS	Microsecond scale	Superior integration capability	High cost Fabrication difficulty	ref.[68,74]

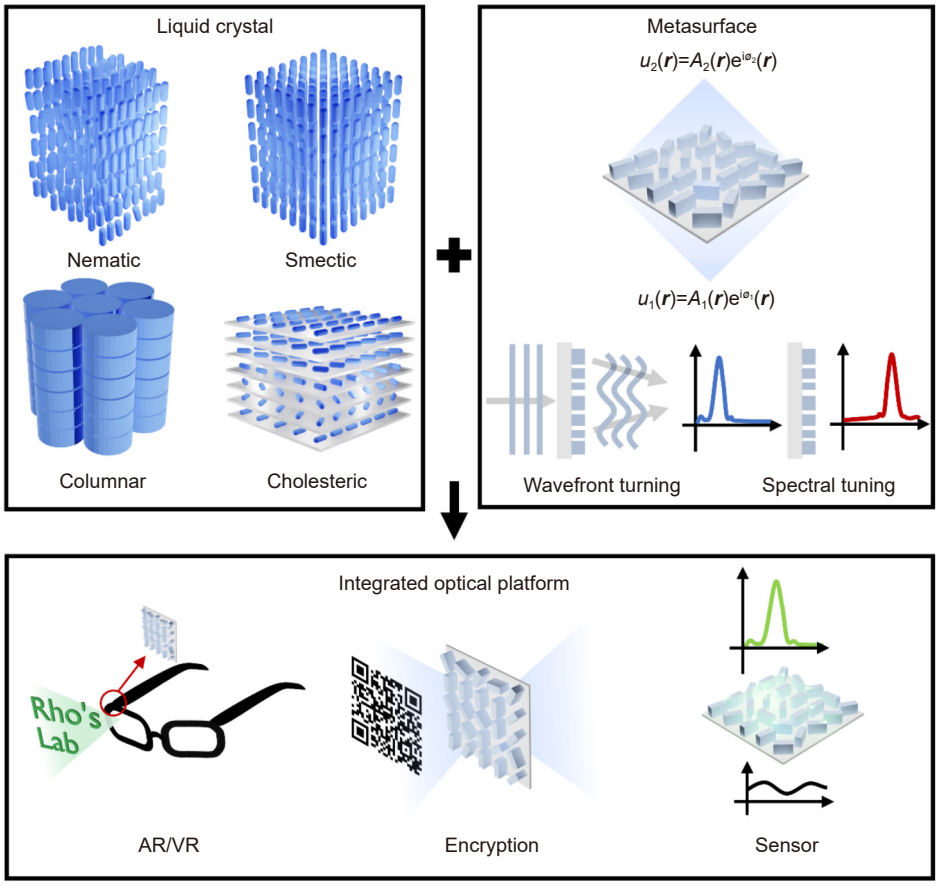

Fig. 1 | Schematic diagram providing an overview of this review. LCs can be categorized into nematic, smectic, columnar, and cholesteric LC based on the alignment of the molecules. Recently, metasurfaces have been integrated with LCs to achieve tunability and this integrated optical platform can be applied to virtual reality (VR), augmented reality (AR), encryption, and sensors.

and spectral tuning [Fig. 1]. Under wavefront tuning, we explore their applications as metaholograms, metalenses, and beam steering, while for spectral tuning, we examine their use in transmissive and reflective tuning, as well as in absorbers. Through this classification, we present select representative research and provide concise explanations of their principles or novelty. Additionally, we highlight the potential of LC-based metasurfaces by including a section on integrated optical platforms. At the end of this review, we summarize our overall contents and discuss the limitations of LC-based metasurfaces in real-life applications.

Liquid crystal

LCs, as their name implies, are intermediate states between crystalline solids and isotropic liquids. In solids, molecules exhibit both positional and orientational order, with specific locations and directions for the centers of mass and molecular axes. In contrast, in liquids, molecules lack preferred positions and directions. In solids, molecules can undergo slight shifts in position and orientation, but they are typically anchored to specific lattice points, moving in relation to the perfect geometric lattice. In the liquid state, molecules freely disperse throughout the sample, and their centers of mass move in random directions. Beyond solids and liquids, there exist other condensed phases with varying degrees of order. One example is the plastic crystal, where molecules are predominantly fixed in a lattice but can vibrate and rotate freely[83]. When molecules have one axis significantly longer or shorter than the other two, phases with some order in position and orientation can emerge, though this order is not as pronounced as in solids or plastic crystals. These phases are referred to as LC phases, where molecules move around while retaining some degree of order. According to the arrangement of the molecules, LCs can be classified into nematic, cholesteric or chiral, smectic, and disk or columnar phase [Fig. 1].

Liquid crystal types

Nematic

In the liquid state, there is no preferred positional order,

as well as orientational order. In the nematic phase, however, the molecules exhibit a preferred orientational order while still lacking positional order. The long axis of the molecules tends to follow a preferred direction, called the LC director, and is expressed by the unit vector $\boldsymbol{n}$. This LC director generally follows a predetermined direction of LC molecules, but after the application of certain inputs, such as voltages, the director of the molecules changes due to the anisotropy of the dielectric constant and conductivity of the LC. In this system, the LC is regarded as a modulator, with inputs being current and output being the change in refractive index of LC molecules, resulting in the modulation of the light passing through the LC. The larger the input, the larger the tilt angle θ of the directors occurs. The effective refractive index can be calculated using the following equation[84,85]:

$$n_{\rm eff} = \frac{n_0 n_{\rm e}}{\sqrt{n_0^2 \sin^2\theta + n_{\rm e}^2 \cos^2\theta}}, \tag{1}$$

where n_0 and $n_{\rm e}$ represent the ordinary and the extraordinary LC refractive indexes, respectively.

Cholesteric

The cholesteric LC has a preferred orientational order but no positional order, which is similar to nematic LC and is also called chiral state. As its name implies, it has a chiral property. The director orientation is arranged by twisting the director of the nematic state. The orthogonal direction of the twisting long axis is the singular direction, and the structures are arranged in the rotating plane following this direction. Thus, cholesteric LC has a helical arrangement, allowing it to selectively reflect circularly polarized light with the same chirality. The central wavelength of the reflection spectrum ($\lambda_{\rm c}$) is related to the helical pitch (p) of the cholesteric LC, signifying the distance measured along the twist axis over which the director completes a full rotation. The average refractive index ($\bar{n}$) and central wavelength can be calculated using the following equations[86]:

$$\bar{n} = \frac{n_0 + n_{\rm e}}{2}, \tag{2}$$

$$\lambda_{\rm c} = \bar{n}\, p. \tag{3}$$

Smectic

The smectic LC, as its most noticeable feature, exhibits both preferred orientational and positional order, unlike nematic or cholesteric LC. The molecules not only have a specifically aligned director but also form a layered structure. These layers can slide independently of each other, and according to the molecular director in layers, the smectic LC can be classified into different types. For example, when the molecular director is orthogonal to the layers, it is called smectic A. In contrast, when the aligned director is not orthogonal to the layers, it is termed smectic C, resulting in biaxial symmetry. In a smectic B phase, a hexagonal crystalline order is present within the layers[87].

Columnar

The columnar LC represents a category of LC phases where molecules organize into cylindrical structures, unlike the aforementioned phases, which have rod-like molecules. These crystals are categorized based on the packing arrangement of the columns. Figure 1 shows an example of hexagonal columnar LC, and in columnar nematic LC, molecules do not form columnar assemblies but instead float with their short axes parallel. Other columnar LCs exhibit two-dimensional lattice arrangements, including tetragonal, rectangular, and herringbone patterns[88].

Types in metasurface design

Among the various types of LCs, nematic LCs are the most commonly used with metasurfaces, followed by cholesteric LCs as the second most frequently utilized. Nematic LCs overwhelmingly dominate, even among nematic and cholesteric LCs. As previously mentioned, while cholesteric LCs offer possibilities for tuning the reflective wavelength, nematic LCs, capable of tuning polarization through their birefringence property, are the most suitable for utilization in metasurfaces. For example, the most commonly employed structure in metasurfaces is the rectangular PB phase structure, which relies on the difference in response between the long and short axes, resulting in characteristics dependent on incident polarization.

Alignment of liquid crystal

To arrange the LC molecules from disordered state to a preferred orientational order, some of the alignment techniques can be employed, typically involving methods such as rubbing alignment or photoalignment. The coating layer used to align the molecules is called the alignment layer, which is usually made of polyimide (PI)

that is optically transparent and stable. The rubbing alignment typically employs unidirectional mechanical friction on the alignment layer to induce the alignment of the molecular chain or generate groove surface[89–91]. Although this method has been widely adopted in industry and laboratory due to its convenience, there are some drawbacks that it can generate undesired defects such as static electricity, impurities, and mechanical damage of the surface caused by the rubbing process of PI films. As a result, researchers have explored alternative contact-free methods to remove the aforementioned problems, of which photoalignment emerging as one of the most powerful non-contact alignment techniques. In this approach, the photosensitive substrate is utilized to enable it to undergo orientational ordering in response to light irradiation, making it advantageous in new applications such as telecommunications and organic electronics[92].

Wavefront tuning

In recent years, various optical systems have been actively researched to realize next-generation optical devices, including AR/VR and transparent displays. Wavefront tuning is a crucial function in creating these devices, and we can dynamically shape the wavefront by sequentially combining the polarization shifting feature of LC with polarization-multiplexed wavefront shaping metasurface, or using pixel-level modulation schemes by designing each pixelated metasurface to have different optical responses depending on the LC state. In this section, we review the recent progress in research on wavefront tuning using LC-combined metasurfaces, categorized into metahologram, metalens, and beam steering.

Metahologram

Holography is an optical technology that involves recording and reconstructing a wavefront to generate optical images, and this is achieved by locally manipulating the phase or amplitude of scattered electromagnetic waves[93,94]. Conventionally, holographic images have been produced using spatial light modulators (SLMs), but large pixel pitch (several micrometers) of SLMs limits the resolution of reconstructed images, lowers viewing angles, and causes unpredictable high-order diffractions with sampling problems[95,96]. These limitations can be overcome by employing metaholograms, which have a subwavelength periodic length[97–99]. Nevertheless, traditional metaholograms can only record single holographic images once their phase profiles are fixed. To solve these limitations, LCs have been applied to tunable metaholograms[100–103].

Dynamic metaholographic displays that respond to various external stimuli, such as heat or surface pressure, as well as electric fields, have been proposed [Fig. 2(a)][104]. When heat or pressure is applied to the LC, its molecular ordering can be altered by the material flow with volume changes owing to pressure gradients or thermal expansion[69,105,106]. The polarization state of light can be controlled because the effective optical birefringence depends on the molecular ordering. The designed LC cell can vary transmitted polarization from right-circularly polarized (RCP) to left-circularly polarized (LCP) light depending on external stimuli. Since designed metaholograms produce different holographic images under RCP and LCP light, metaholographic displays can switch images in real time with various inputs such as electric bias, finger touch, and heat. Similarly, spin-decoupled helicity-multiplexed metasurfaces have been integrated with pressure-sensitive LCs[107]. The designed structure has been implemented in a finger touch-enabled holographic switching device that converts the helicity of incident light using LC depending on the pressure. However, these devices can only exhibit two pieces of information because they work only under RCP and LCP light.

Li et al. have demonstrated an electrically controlled digital metasurface device (DMSD) for light projection displays as shown in Fig. 2(b)[81]. The numeric indicator display, realized by this device, can showcase ten pieces of information using seven switchable metasurface pixels. Each metasurface pixel can be electrically turned on and off by manipulating the relative phase between adjacent odd and even columns in each metasurface. The relative phase of each column can be expressed as $\Delta\varphi$. In this study, there are two phase factors: the geometric phase ($\Delta\varphi_g$) and the propagation phase ($\Delta\varphi_p$). Because rectangular-shaped meta-atoms are used in this study, the geometric phase only depends on the difference in rotating angle ($\Delta\theta$) of the meta-atoms in each column. As shown in Fig. 2(b), $\Delta\varphi_g = 2\Delta\theta = \pi$ is fixed in this study. $\Delta\varphi_p$ can be modulated by coating different materials in each column with refractive indices of n_a (LCs) and n_b (PMMA trenches). Here, n_b is a fixed value of 1.5, while n_a, the only variable, can be tuned from 1.53 to 1.92 by electrical input. Consequently, when no input voltages are applied, $n_a = 1.92$ and $n_b = 1.5$, resulting in an additional propagation phase, so that $\Delta\varphi = \Delta\varphi_g + \Delta\varphi_p = 2\pi$, leading to completely on states. As the applied

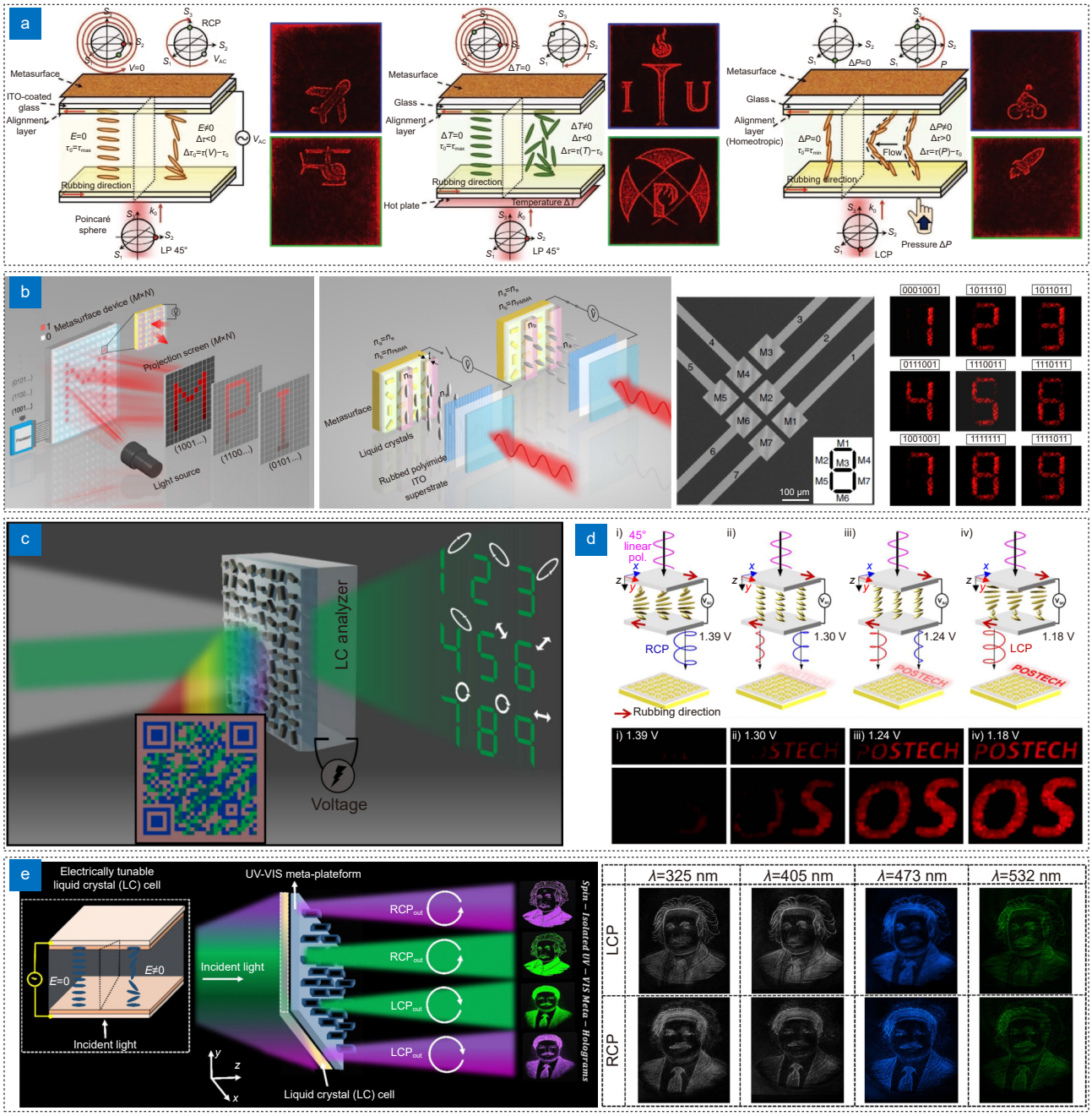

Fig. 2 | Tunable metaholograms with LC. (**a**) Dynamic metaholographic displays that respond to various external stimuli. The left image shows a voltage-responsive display, the middle image shows a heat-responsive display, and the right image shows a touch-responsive display. (**b**) An electrically-controlled DMSD for light projection. The left two images show the DMSD device and its working principle. The right two images show an SEM image of the DMSD and experimental results of the DMSD with independent control of seven electrodes each. (**c**) Schematic of the security platform using an electrically tunable vectorial holographic device. (**d**) Chiral metasurfaces integrated with LC enable precise control of hologram intensity, offering the ability to switch between fully "on" and "off" states. The top images show illustrations of the adjustable intensity of holograms utilizing chiral metasurfaces. Upon illumination of LCs with 45° linearly-polarized light, an output polarization state of RCP is observed at a voltage of 1.39 V, and a transition to LCP state occurs at a voltage of 1.18 V. The bottom images show the measured results when the applied voltages were (i) 1.39, (ii) 1.30, (iii) 1.24, and (iv) 1.18 V. (**e**) Schematic of the broadband metahologram operating in both the UV and visible regions. The image on the right shows the experimental results of the designed broadband metahologram. Figure reproduced with permission from: (a) ref.[104], © 2020 John Wiley and Sons; (b) ref.[81], (c) ref.[108], (d) ref.[109], under a Creative Commons Attribution 4.0 International License; (e) ref.[110], © 2023 Royal Society of Chemistry.

voltages increase, n_a decreases, eventually reaching n_a = 1.53, resulting in $\Delta\varphi = \Delta\varphi_g + \Delta\varphi_p = \pi$, signifying totally off states. By controlling seven independent metasurface pixels, reconstructed holographic images, including numbers from 0 to 9 (0 is not shown in the figure), have been demonstrated [Fig. 2(b)]. Although this approach can produce multiple images, the need for an array of metasurface pixels hinders its applications because of fabrication or cost issues.

Kim et al. have proposed an electrically tunable vectorial holographic device that can exhibit multiple images without using a metasurface array [Fig. 2(c)][108]. The proposed meta-atoms can act as both a Mie-resonator and a localized half-wave plate. Thus, this device can simultaneously produce a structural color print under unpolarized white light and generate polarization-encoded metaholograms when exposed to coherent laser illumination. This vectorial holography has more degrees of freedom because it works under elliptical polarization, while conventional metasurfaces-based holograms only work under RCP and LCP. Elliptical polarization can be generated by the superposition of RCP and LCP in various ways, and this device produces multiple images depending on the arbitrarily defined polarization states. To miniaturize the device and enable active control based on electrical bias, an LC modulator is integrated in place of the polarizer and retarder. Two-level security applications have been demonstrated using this concept. When the QR code is scanned, the corresponding voltage values are transmitted, and the receiver can decipher the code through the hologram image. This research shows the potential of LC-integrated metasurface, which can be applied to practical devices.

While a metahologram can display multiple images, there had been no research demonstrating continuous image tuning, as previous studies had only shown discrete image tuning. Yang et al. demonstrated LC-integrated chiral metasurfaces as a method to continuously control intensity between fully "on" and "off" states [Fig. 2(d)][109]. Conventional LC-based metaholograms possess limitations in achieving a complete off-state. Employing fully elliptically polarized states, encompassing both RCP and LCP, offers enhanced degrees of freedom for tunable metasurfaces. To achieve complete absorption of RCP within the visible range, gap-shifted split-ring resonators utilizing multilayer structures consisting of metal and dielectric materials have been proposed to generate strong gap-plasmonic responses. Applying a voltage of 1.39 V to the LC, RCP is incident on the chiral metasurfaces, and the resultant image exhibits nearly negligible intensity with 99.9% of the incident light absorbed. Conversely, by applying a voltage of 1.18 V to the LC, LCP is incident, leading to the reconstruction of a vivid metaholographic image.

So far, most research on metaholograms has focused on the polarization-tuning mechanism to overcome the limitations of information capacity. Broadband metaholograms are also a novel approach to address this information capacity limit. Asad et al. have proposed a broadband metahologram operating in both the ultraviolet (UV) and visible regions, which exhibits different images for the RCP and LCP [Fig. 2(e)][110]. Similar to previous research, LCs enable this device to switch between RCP and LCP freely. There has been little research on UV metaholograms due to their low efficiency and fabrication difficulties. However, this group selected silicon nitride (Si_3N_4) for broadband metahologram operating in both the UV and visible region because this material possesses a large band gap energy of 5.9 eV, a high refractive index, and a low extinction coefficient. This group has demonstrated multiple holographic images in broadband region, showcasing how the integration of the unique properties of LCs can greatly enhance system performance.

Despite these outstanding performances, several problems remain and limit functional utilization. While the novel LC-based approaches which utilizes polarization states or broadband properties to provide a greater degree of freedom for information storage limits offer potential, it remains inadequate for practical technological utilization. Furthermore, even when increasing the number of holographic images through these approaches, addressing efficiency degradation and crosstalk between multiple images remain a crucial challenge for future holographic devices.

Metalens

Metalenses, thin and flat lenses consisting of nanostructure arrays, have attracted significant attention in recent years due to their potential for miniaturizing optical systems, a crucial aspect for next-generation applications, including AR/VR[111,112] and bio-optics[113,114]. However, these thin and flat lenses still face challenges similar to conventional lenses, such as chromatic aberration and high NA. To overcome the limitations, numerous metalenses with diverse functionalities have been proposed,

including multi-focusing[115–117], broadband, chromatic aberration correction[118–120], and wide FOV lenses[121–124]. Particularly, achieving active performance such as multi-focusing with metalenses for practical applications presents a challenge due to their passive nature. Various methods have been utilized to realize the dynamic response of metalens, with the integration of LCs being one of the actively explored approaches.

Compared to conventional lenses which inevitably have bulky systems to achieve the control of the focal length, varifocal metalenses integrated with LCs are relatively small and compact, which is a good advantage for various applications. Fan et al. have proposed a varifocal metalens integrated with twisted nematic (TN) LCs which has improved response time and high imaging quality compared to conventional tunable lenses [Fig. 3(a)][82]. TN LCs, which can rotate polarization angle of 90°, are utilized to electrically modulate the polarization of incident light between *x*- and *y*-polarization states, while bifocal metalens is designed to shift the focal length depending on incident polarization states. Each unit cell of metalens is selected to provide different phase distributions in *x*- and *y*-polarized light, by properly changing their lengths and widths. This design shows not only a rapid response time of sub-millisecond level, but also high focusing efficiencies and the full width at half maximum close to diffraction limit at each focal point, meaning that high imaging quality can be shown.

Badloe et al. have proposed an LC-cell combined tunable bifocal metalens achieving high focusing efficiency with the design of the metasurface using both propagation phase and geometric phase to overcome restrictions of each method [Fig. 3(b)][30]. The dimensions of each meta-atom were carefully selected to cover the 2π range for the propagation phase, while also considering function as half-wave plates. In the sequentially combined LC-integrated metalens, RCP and LCP states are produced from the incident linearly polarized light through the LC cell at 1.1 and 1.3 V, and then each of them can generate focal point at 3.7 and 7.5 mm through the bifocal metalens. As a result, focal spots exhibiting profiles close to perfect Airy disks and high Strehl ratios were achieved at each focal point, which indicates diffraction-limited performance of the lens. As shown in the right panel of Fig. 3(b), imaging using this bifocal metalens was also demonstrated, with the modulation transfer function (MTF) of the metalens closely matching that of the diffraction-limited MTF at each focal point.

Hu et al. have demonstrated electrically tunable metalens by combining LCs with geometric phase metasurface, constructing an LC-based tunable platform with simple processing and increased polarization conversion efficiency [Fig. 3(c)][125]. LC-based wave plate designed to dynamically implement variable phase retardation is used to convert circularly polarized light emitted from the encapsulated metasurface into variable elliptically polarized light. The LCP and RCP channels can be switched by filtering with a linear polarized analyzer applied in an angle of 45° with the in-plane azimuthal angle of LC molecules. Using vector decomposition with non-interleaved metasurfaces[126] as a multiplexing method, switching two orthogonal helicity channels with two different focal points can be achieved. The packaging strategy of wrapping meta-atoms in PMMA is selected over direct LC wrapping strategies, which can achieve larger refractive index contrast and higher polarization conversion efficiency. Due to the broadband characteristic of the geometric phase, focusing on multiwavelength can be performed.

Instead of using methods to control the polarization of light through LC, an alternative approach involves adjusting the LC orientation to modulate the local refractive index surrounding the metasurface, consequently changing the phase delay. Bosch et al. have proposed a tunable zone plate metalens, whose focal distances can be continuously manipulated by changing a rotation angle θ of LC molecules [Fig. 3(d)][127]. The meta-atoms supporting Mie-type resonant modes encapsulated in nematic LC are engineered to produce a phase delay profile corresponding to zone plate lens, whose focal distance can be modulated by changing the refractive index of the surrounding LC cell. Compared to the discrete bifocal lens which can shift between only two focal lengths, a varifocal metalens is designed to provide multiple focal lengths between two values at the corresponding intermediate LC molecule rotation angles $0° < \theta < 90°$. To achieve this, the phase of each meta-atom is numerically optimized to change near-linearly with θ at five values within the range of $0° < \theta < 90°$. As depicted in the simulation results shown in Fig. 3(d), increasing the amplitude of a bias voltage V_0 leads to an increase in the rotation angle of LC molecules, resulting in slight changes in the phase profiles of metasurface and thus a continuous decrease in the focal length.

Besides its ability to adjust the focal length of the metalens using LC, some research has also suggested new

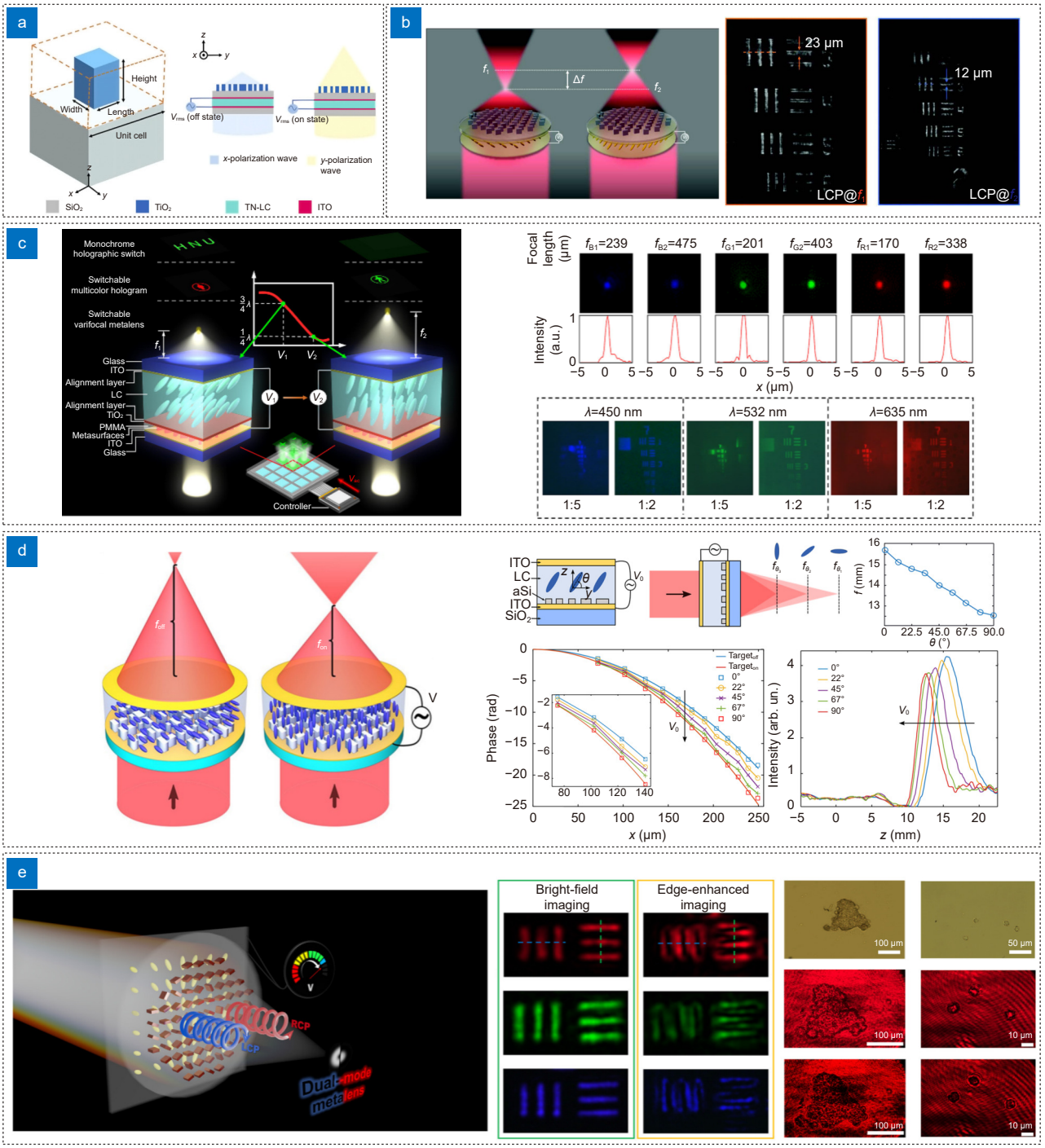

Fig. 3 | Tunable metalenses combined with LCs. (**a**) Schematic of the varifocal metalens integrated with TN LCs designed by sweeping lengths and widths of the meta-atom. (**b**) Schematic of an LC-cell combined bifocal metalens. The right images were captured by using the bifocal metalens in each focal plane of f_1 and f_2 with LCP and RCP incident light, respectively. (**c**) Schematic of the electrically tunable platform using metasurface integrated with LCs. The right images show the demonstration of the electrically tunable metalens using the platform. Focusing and imaging were demonstrated at each focal plane at the target wavelength of 450, 532, and 635 nm. (**d**) A varifocal metalens encapsulated in an electrically biased LC cell. The focal length continuously varies by changing bias voltage between its "off" and "on" values. (**e**) Schematic of a tunable metalens switching from bright-field mode to edge-enhanced imaging mode depending on incident polarization beam. The middle images show captured images of the resolution target obtained through each mode for RGB wavelengths. The right images show captured images of biological samples by bright-field optical microscope (top), bright-field mode in metalens (middle), and edge-enhanced imaging mode in metalens (bottom). Figure reproduced with permission from: (a) ref.[82], © 2020 Optica Publishing Group; (b) ref.[30], under a Creative Commons Attribution 4.0 International License; (c) ref.[125], (d) ref.[127], © 2021 American Chemical Society; (e) ref.[128], © 2023 American Chemical Society.

dynamic functionalities for various applications, including biological imaging. Badloe et al. have demonstrated electrically tunable metalens integrated with LC cell which can switch from bright-field mode to edge-enhanced imaging mode [Fig. 3(e)][128]. By combining propagation phase and geometric phase, conventional hyperbolic lens phase profile and spiral phase profile can be encoded into a single metalens. To prove the advantage of using metalens over conventional lens systems that all complex information can be obtained, bioimaging with small amplitude fluctuations is demonstrated with designed metalens.

However, there is still a long way to go before these innovative concepts can be applied to practical devices. First, some problems of the metalens itself, such as aberrations, broadband operation, low focusing efficiency, and large-scale design, need to be resolved. Furthermore, maintaining high focusing efficiencies on both states is essential in switchable imaging systems. Increasing the modulation number of focal points of varifocal metalens could also be an interesting issue.

Beam steering

Beam steering is a technique used to dynamically direct a beam in a desired direction, which is highly required in applications such as LiDAR, displays, laser machining, and optical communications. Mechanical approaches, including rotating mirrors[129] and MEMS mirrors[130,131] have conventionally been used as beam steering methods. Concurrently, there has been an active exploration of non-mechanical methods, with LC-based devices gaining a significant attention for their lightweight, compact, and cost-effective nature compared to other techniques. LC-based beam steering devices have commonly utilized the tunability of LCs in conjunction with various optical elements, which can function as blazed gratings, Bragg gratings, and prisms[132]. Recently, metasurfaces have been integrated into LC-based beam steering devices, offering the potential for achieving wide FOV and high efficiency.

Komar et al. have demonstrated a dynamically switchable beam deflector in the visible region using a Huygens dielectric metasurface infiltrated with LCs [Fig. 4(a)][133]. By heating the LC from 25 °C to 60 °C, a transition of the LC arrangement occurs from nematic to isotropic state, which leads to a refractive index change. The embedded Huygens metasurface is designed to transmit light straight through in nematic state, while deflecting it at a specific angle in isotropic state. Different-sized nanodisks are employed to introduce the desired phase delays, covering a range of 2π with satisfying Huygens' condition in isotropic state, and creating a phase gradient that functions as a binary blazed grating. As shown in the left panel of [Fig. 4(a)], the power distribution among the diffraction orders of the transmitted light through the device is changed by varying the temperature and altering the LC state. With the LC state shifted from nematic to isotropic as the temperature rises, the intensity of the zeroth order decreases while the intensity of the first order increases. The device effectively controls the amount of beam deflection at the angle of 12° at the working wavelength of 745 nm.

Beam steering can be achieved non-mechanically using SLM, however, the widely used LC-based SLM suffers from large pixel sizes and consequently small FOV issues. To alleviate this problem, a phase-only transmissive SLM with miniaturized pixel size using Huygens metasurface has been demonstrated [Fig. 4(b)][134]. In this work, the desired phase accumulation can be implemented by changing the LC arrangement and inducing local environment and resonance changes of the nanoantennas, rather than modulating phase delay solely by LC layer. This enables a reduction in the LC cell thickness, leading to decreased pixel sizes and resolving the issue of limited FOV. The radius of the TiO_2 nanoantennas is optimized to satisfy Huygens' condition, and the phase retardation of the light transmitted through the optimized unit cell is calculated for LC molecule orientations of 0°, 45°, and 90°. The results showed evenly spaced phase retardation of approximately 2π/3 between each other and similar high transmittance at three states within the wavelength range of 660–670 nm, indicating the possibility of designing a three-level-addressing scheme. A beam steering SLM is designed with three nanoantennas per pixel, which accommodate phase broadening and fringing field effects[65]. The device is fabricated with 28 individually addressable electrodes, acting as a diffraction grating, and the diffraction angles can be changed by adopting different electrode-addressing configurations. By using a three-level-addressing scheme, the device achieves effective suppression of the 0th order and the +1th order while enhancing the −1th order to values exceeding 15% at the deflection angle of 11°. To mitigate the shortcomings arising from a small sample size, a larger device is also designed. Although it cannot alter the deflection angle and is limited to reversing the deflection

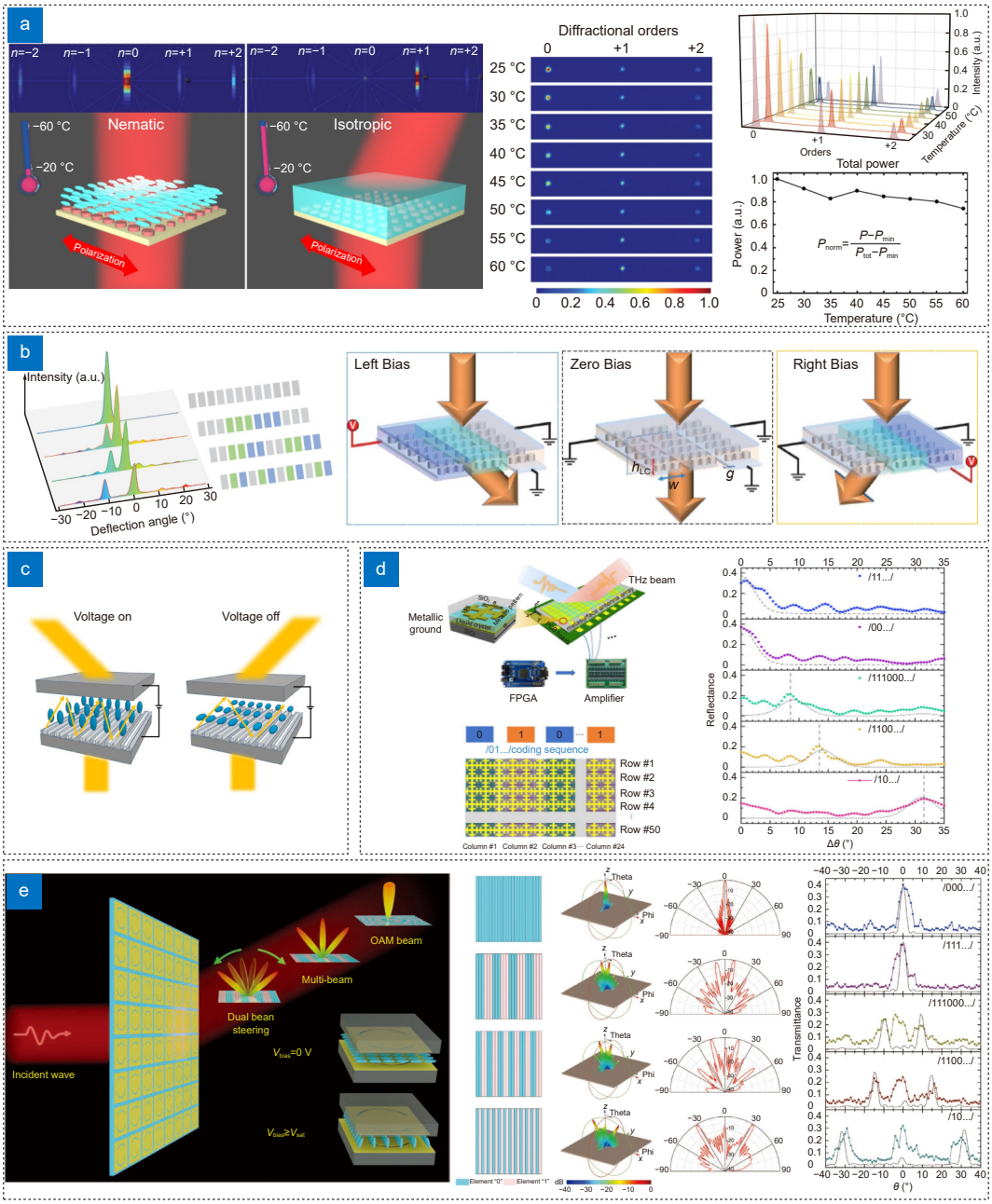

Fig. 4 | Metasurface-based dynamic beam steering devices combined with LCs. (**a**) The left images show the concept of a metasurface-based beam-switching device. It transmits light straight through in nematic state and deflects it at a fixed angle at isotropic state. The right shows 2D images and measured intensity of three main diffraction orders (0, +1, +2) for different temperatures. The total power of transmitted light varying with temperature is also measured. (**b**) The left image shows a three-level-addressing scheme of beam steering device with tunable deflection angle. The right image shows the concept of large aperture device with integration of active-matrix electrodes. (**c**) Schematic of LC-tunable metasurface using inverse design. A designed grating deflects incident light to the target angle in the opposite direction depending on the voltage “on” and “off” states. (**d**) The left image shows the schematic of a programmable metasurface performing THz beam steering. Shifting the applied coding sequence changes the beam deflection angle. The right image shows the measured and calculated distribution of the reflected beam for the applied five coding sequences at 672 GHz. (**e**) The left image shows the schematic of the digital coding metasurface using a MIM resonator and CASR pattern, performing various THz beam manipulation functions including dual beam steering. The middle images show the coding patterns and simulated 3D, and 2D scattering patterns for dual beam steering at 0.408 THz. The rightmost figure shows a comparison between the measured and simulated scattering patterns of the transmitted beam for five different coding sequences. Figure reproduced with permission from: (a) ref.[133], © 2018 American Chemical Society; (b) ref.[134], © 2019 The American Association for the Advancement of Science; (c) ref.[135], © 2020 American Chemical Society; (d) ref.[136], © 2020 AIP Publishing; (e) ref.[137], © 2021 John Wiley and Sons.

direction, it significantly improves deflection efficiency reaching 36% at 660 nm.

To make an active beam steering device with both high device efficiencies and high deflection angles, a method of applying inverse design to LC-based metasurface has also been proposed [Fig. 4(c)][135]. The optimized device consists of a single silicon grating embedded in the LC layer, along with two supportive TiO_2 gratings on the top and bottom, switching the beam deflection by applying voltage to the LCs. To maintain high performance across multiple refractive-index states using a single geometrical structure, it requires extensive computational optimization with numerous degrees of freedom. The adjoint method is utilized to effectively optimize many small-scale degrees of freedom, combining with Particle swarm optimization as a global optimization algorithm to deal with larger geometrical parameters such as layer thickness and periodicity of the structure. By utilizing multiple gratings optimized for each specialized role, it is possible to find a structure achieving very high switching angles with having near-unity switching efficiency. Consequently, the highest deflection-angle design achieves a large deflection angle from −72° to +72°, simultaneously reaching large diffraction efficiencies of 62% and 76% in each state.

Active beam steering techniques are also highly demanded in THz wave applications such as communication, security screening, biological imaging, and astronomy. For the phase manipulation of THz beams, digital coding and programmable metasurfaces have been widely adopted, which use binary coding elements with several discrete phase responses and switch the state of each coding element dynamically. Wu et al. have demonstrated a programmable metasurface performing a THz beam steering with a tunable LC layer [Fig. 4(d)][136]. The designed beam steering device is composed of a 24-column linear array with each column containing 2×50-unit cells, and each unit cell has a metal-insulator-metal (MIM) resonator structure with the Jerusalem cross patterns on its top and pixelated rectangle patch on its bottom metallic layers. The refractive index change of the LC layer induced by applying an electric field leads to a shift in the absorption frequency, thus allowing modulation of the reflection amplitude and phase for each coding element. In this study, a relative phase difference of π is achieved by applying appropriate bias voltage (0 V and 40 V), which is half of the range of 2π due to the low filling factor of the top pattern of the unit cell. As a result, the 1-bit coding can be defined with the 0 and 1 coding states which have a relative phase difference of π and the same reflection amplitude. The deflection angle can be adjusted by modifying the coding sequences using a field programmable gate array (FPGA) board, which in turn alters the periodicity of the subarray. At the working frequency 672 GHz, the deflection angle reached 31.5° but it has low beam deflection efficiency, due to several factors such as low reflection efficiency, low filling factor of unit cell pattern, and significant specular reflection.

A THz beam steering using a transmissive digital coding metasurface with an LC layer has also been proposed, incorporating a MIM resonator and complementary asymmetrically split ring (CASR) pattern on the metallic layer [Fig. 4(e)][137]. The CASR is employed to utilize the Fano resonance which can be excited by symmetry breaking, making the high-Q resonance and enabling a large phase difference. By carefully selecting the dimensions of the CASR structure, almost the same transmittance and the maximum relative phase difference of near π are achieved at 0.408 THz, meaning that 1-bit digital coding metasurface can be designed. As depicted in Fig. 4(e), a dual beam steering is demonstrated by varying the coding patterns, resulting in the direction of the transmitted THz beam steered from 0° to 31.9°. However, for practical beam steering applications, it is crucial to enhance deflection efficiency and expand the FOV, making it essential to focus future research efforts on maximizing these values. In specific applications such as LiDAR, some other factors including high frame rates, high spatial resolution, and economical on-chip integration should also be considered.

Spectral tuning

Spectral tuning, another significant functionality of metasurfaces, allows for the modulation of the transmissive or reflective properties of electromagnetic waves at specific wavelengths. By carefully designing the meta-atoms, desired resonance effects can be achieved, enabling applications such as color filters and sensors. In this section, we summarize recent research on spectral tuning based on LC-combined metasurfaces, categorized into transmissive or reflective tuning and absorbers.

Transmissive or reflective tuning

Exploiting the anisotropy of LC with various inputs, the resonance in meta-atoms can be arbitrarily modulated, enabling the tuning of transmissive or reflective spectra.

Research on transmissive or reflective tuning in LC-based metasurfaces has mainly been conducted in the visible region, whereas research in the near-infrared (NIR) and THz regions is relatively less extensive. Therefore, we have divided this section into the visible region as well as the NIR and THz region.

Visible region

Most research on transmissive or reflective tuning by LC-based metasurfaces has been conducted in the visible region, with a primary focus on designing a colorful gamut through resonance mode tuning. Color displays are indispensable in our daily lives, such as those found on smartphones, tablets, televisions, and other video displays. However, conventional dye-based color displays have critical issues, such as color fading and wavelength-limited resolution[138]. Thus, color generation based on metasurface with the advantages of ultrahigh resolution and natural colors has been actively researched, including structural coloration and color filtering[139–141]. However, the versatility of conventional metasurface-based color generation is limited[142]. To overcome this limitation, dynamically tunable color generation is necessary, and LCs are promising materials to dynamically control the color.

Xie et al. proposed a dynamic plasmonic color filter based on aluminum grating metasurface combined with LCs by controlling the applied voltage with a range from 0 to 4 V [Fig. 5(a)][143]. At a voltage of 0 V being applied, the polarization state of the incident light is altered to align parallel to the grating vector, while the initial incident direction is parallel to the grating stripes. In brief, the transverse magnetic (TM) polarization effect is attained at an applied voltage of 0 V. On the other hand, the transverse electric (TE) polarization effect is attained when a voltage exceeding 4 V is applied since the application of an external voltage prevents the rotation of the incident light's polarization state. The color modulation correlates with the fluctuations in TM and TE polarizations according to small variations of the applied voltage [Fig. 5(a)]. Aluminum is selected because it has low transition loss, which can generate more vivid colors, while metals generally have a high loss. However, the color tuning range is not enough for color displays.

Lee et al. implemented widely separated color generation by using an asymmetric lattice nanohole array of metasurface [Fig. 5(b)][144]. Depending on the structural parameters, such as the film thickness, hole shape, and inter-hole spacing, the resonance property can be precisely selected. Additionally, in the case of the plasmonic asymmetric nanostructure, the color resonance mode varies based on the polarization state of the incident light. By appropriately selecting the structural parameters and using a combination of LCs, they experimentally demonstrated a color-tuning shift of over 120 nm. Two primary colors can be generated by applying voltages of 0 V and 5 V, respectively, and the mixed states of the two primary colors can be continuously generated by adjusting the applied voltage. Although the color tuning range was improved significantly, it was still not enough to cover the RGB region.

Driencourt et al. demonstrated an electrically tunable color filter that can encompass over 70% of the color gamut found in conventional RGB filters [Fig. 5(c)][145]. The achieved tuning range results from the combination with birefringent-induced colors transmitted by a plasmonic nanostructure and a thin LC cell. Specifically, the plasmonic structure yields the color red supported by silver nanowire, blue from the LC cell, and green from the integration of two-color states. This single tunable filter covering the RGB region boosts the possibility of display miniaturization and high-resolution display.

Covering the RGB region via a single pixel has been demonstrated in the case of both structural coloration and color filtering. Franklin et al. proposed a reflective plasmonic nanostructure capable of producing the full RGB color basis set [Fig. 5(d)][146]. The resonant wavelength is determined by the effective refractive index of grating coupled surface plasmons (GCSP) modes which are affected by the alignment of LC near the plasmonic surface. Polarized light from the linear polarized glass superstrate, indium tin oxide (ITO), and a rubbed PI film enters the LC layer and excites GCSP on the aluminum surface. As a result, different applied voltages cause variations in LC orientation, resulting in different plasmonic modes and transitions in color. However, even though a single pixel can cover the full RGB region, LCs-powered structural color generation based on plasmonic metasurfaces is still hindered by unavoidable ohmic losses in the visible region, which can lead to performance degradation. Additionally, black and gray states are significant for complete displays as they can control important factors such as brightness and contrast, which conventional approaches have not been able to implement.

Badloe et al. constructed a tunable all-dielectric metasurface, which provides full-color reflective displays and

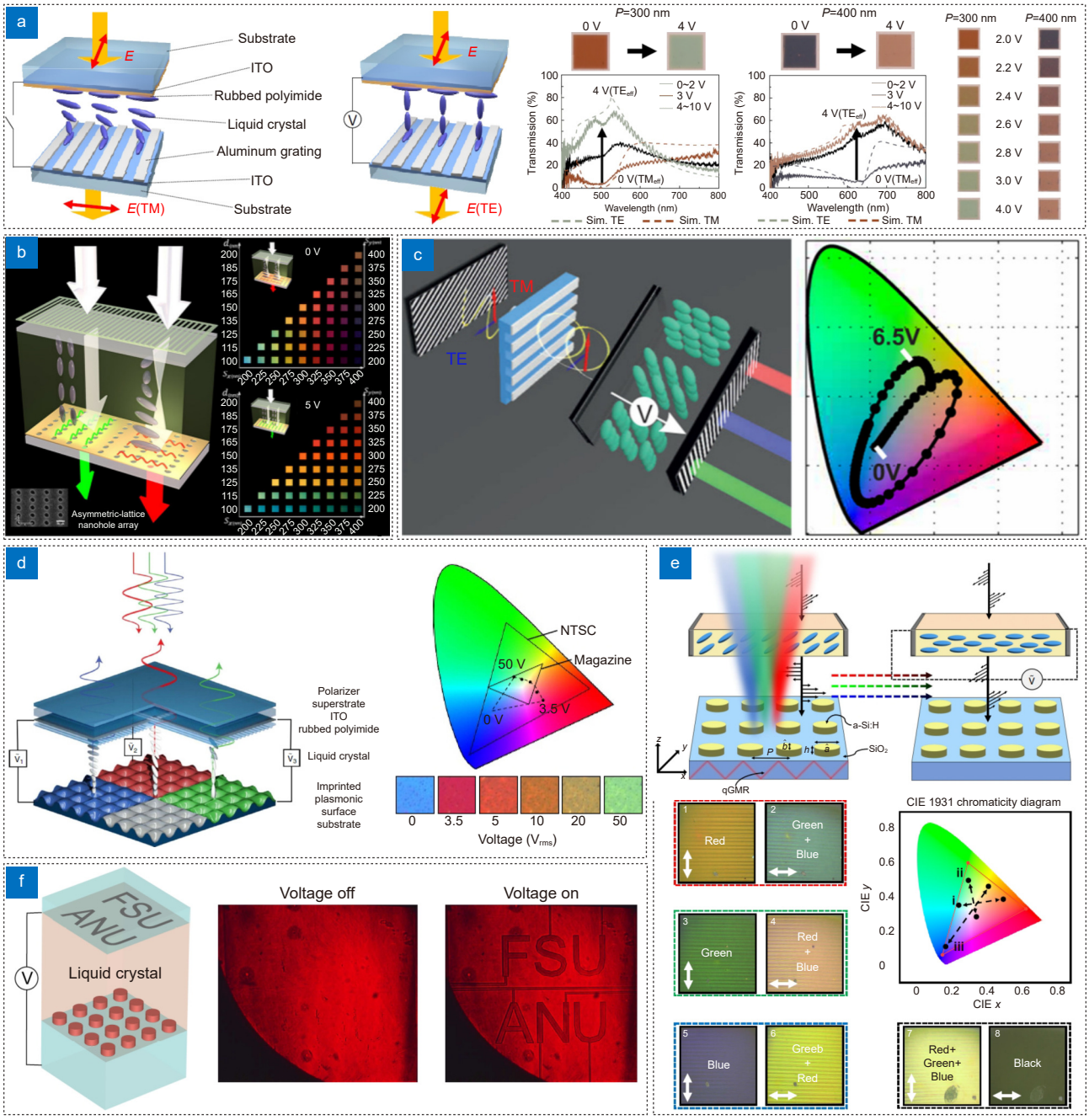

Fig. 5 | Color generation metasurfaces combined with LCs. (**a**) The left images show a schematic of aluminum grating metasurface integrated with LC. The right images show experiment results of Al grating metasurface with incrementing the applied voltage from 0 V to 10 V. (**b**) Schematic of wide tuning range color filter and optical photographs of proposed structure for the initial voltage of 0 V and the saturated voltage of 5 V. (**c**) The left image shows a schematic of proposed color filter achieving a color coverage exceeding 70% of the sRGB color gamut. The right image shows the CIE chromaticity diagram of the transmitted colors for the proposed structure. (**d**) The left image shows a schematic of the LC plasmonic device producing full RGB color. The right image shows the CIE chromaticity diagram of the LC plasmonic device and that of the comparative standard. (**e**) The top image shows a schematic of tunable all-dielectric LC system. The bottom image shows experimental results with rotated subpixels and the CIE chromaticity diagram of the all-dielectric LC device. Under an LP axis of 90°, the intended primary color is generated, while at an LP axis of 0°, successful mixing of two colors is achieved. (**f**) The left image shows a schematic of the switchable transparent displays which can be turned on and off. The right image shows experimental images of the device at the applied voltage of 0 and 20 V. Figure reproduced with permission from: (a) ref.[143], © 2017 Optica Publishing Group; (b) ref.[144], © 2017 American Chemical Society; (c) ref.[145], © 2020 American Chemical Society; (d) ref.[146], (e) ref.[147], under a Creative Commons Attribution 4.0 International License; (f) ref.[149], © 2019 American Chemical Society.

a nearly linear transition from vivid, saturated "on" states to deep, black "off" states. [Fig. 5(e)][147]. Two factors determine the possibility of vivid colors: the material and the geometry of the meta-atoms. This group used low-loss hydrogenated amorphous silicon for the meta-atoms[148], which leads to stronger Mie scattering effects. Therefore, more vivid color can be generated because of a high refractive index and low extinction coefficient in the visible region. This group chose an ellipsoidal-shaped meta-atom due to its optimum reflectance and LP dependency. By integrating polarization-dependent anisotropic meta-atoms and an LC modulator, tunable reflective metasurfaces have been easily demonstrated. The modulation of the LP axis of the meta-atoms, transitioning from alignment along the long axis to the short axis, enabled the attainment of black states and grayscale colors.

Figure 5(f) shows another example of structural color using LCs. Zou et al. demonstrated switchable transparent displays in the visible region by integrating a Mie-resonant silicon metasurface into a nematic LC cell[149]. The display can be turned on and off through applied voltage from 0 to 20 V. This group realized an absolute transmission modulation of 53% at a wavelength of 669 nm by utilizing a photoalignment material, which can increase the accuracy of the LC alignment.

However, the color generation by the LCs has two main drawbacks[138]. First, continuous and constant power is needed to stay in the current color state. Second, the microscale of the LC cells and additional polarizers make the device hard to fabricate, miniaturize, and increase the reflection efficiency. These problems have to be solved for the next-generation LC-based metasurface displays.

Near-infrared and terahertz region

In the NIR and THz region, the majority of research on LC-based metasurfaces has focused on utilizing high-Q resonance modes, which can be applied in sensing and imaging. For instance, Sharma et al. have demonstrated the electrical tuning of nonlocal second-harmonic generation by combining a nonlinear metasurface with an LC layer in NIR region [Fig. 6(a)][150]. The polarization-dependent surface lattice resonance, with its high-Q resonance characterized by a narrow spectral width, results in strong nonlocal second-harmonic generation. LC allows for the electrical control of polarization within the system, thereby enhancing or attenuating the second harmonic signal, effectively providing active control of the nonlinear device. This concept has potential applications in optical signal processing and sensing.

Another instance of high-Q resonance can be seen in the work of Ni et al., who implemented a multi-dimensional light field encoder capable of simultaneously measuring the polarization and spectrum of NIR light [Fig. 6(b)][151]. This group utilized electrically tunable anisotropic high-Q-GMR by using LC. Photodetectors can only measure the intensity of light. Therefore, this group calculated the measured intensity using a photodetector after an unknown signal passed through the LC-combined metasurface, adjusting the N numbers of applied voltage. By fitting the measured intensity information to the proposed matrix equation, it is possible to simultaneously reconstruct the polarization and spectrum of the incident light. This concept also has applications in sensing and bioimaging.

Research utilizing LC for tuning anisotropy and chirality is also conducted in the THz range. Zhao et al. have proposed electrical tunable anisotropy and chirality in the THz region by rotating the optical axis of LC [Fig. 6(c)][152]. When the optical axis of LC is parallel to the optical axis of the meta-atom, the anisotropy of the device is enhanced. Conversely, when the axes are orthogonal, the anisotropy is canceled, resulting in an over 180° range of phase shift. Furthermore, between the parallel and orthogonal orientations, chirality arises due to the breaking of mirror symmetry, which can find applications in polarization imaging and chiral spectroscopy.

Furthermore, Shen et al. have demonstrated active Fano resonance cloaking in the THz region using anisotropic split-ring-shaped meta-atoms [Fig. 6(d)][153]. This ring structure has two gaps on both sides. By electrically tuning the polarization state with LC, when the polarization is orthogonal to the two gaps, a sharp Fano resonance occurs. When it is parallel, a high-transmissive state is achieved, effectively enabling Fano resonance cloaking.

So far, we have discussed research on tuning high-Q resonance modes with LC-based metasurfaces. Another attempt, conducted by Wang et al., involved examining the relationship between the orientation of the LC axis and the geometry of rectangular meta-atoms in NIR and visible region[Fig. 6(e)][154]. Through electrical tuning of LC, longitudinal and transverse polarization is incident on the metasurface, and the ratio between the length and width of the metasurface varies from 1:1 to 1:5. When the ratio is 1:1, the width and length are the same,

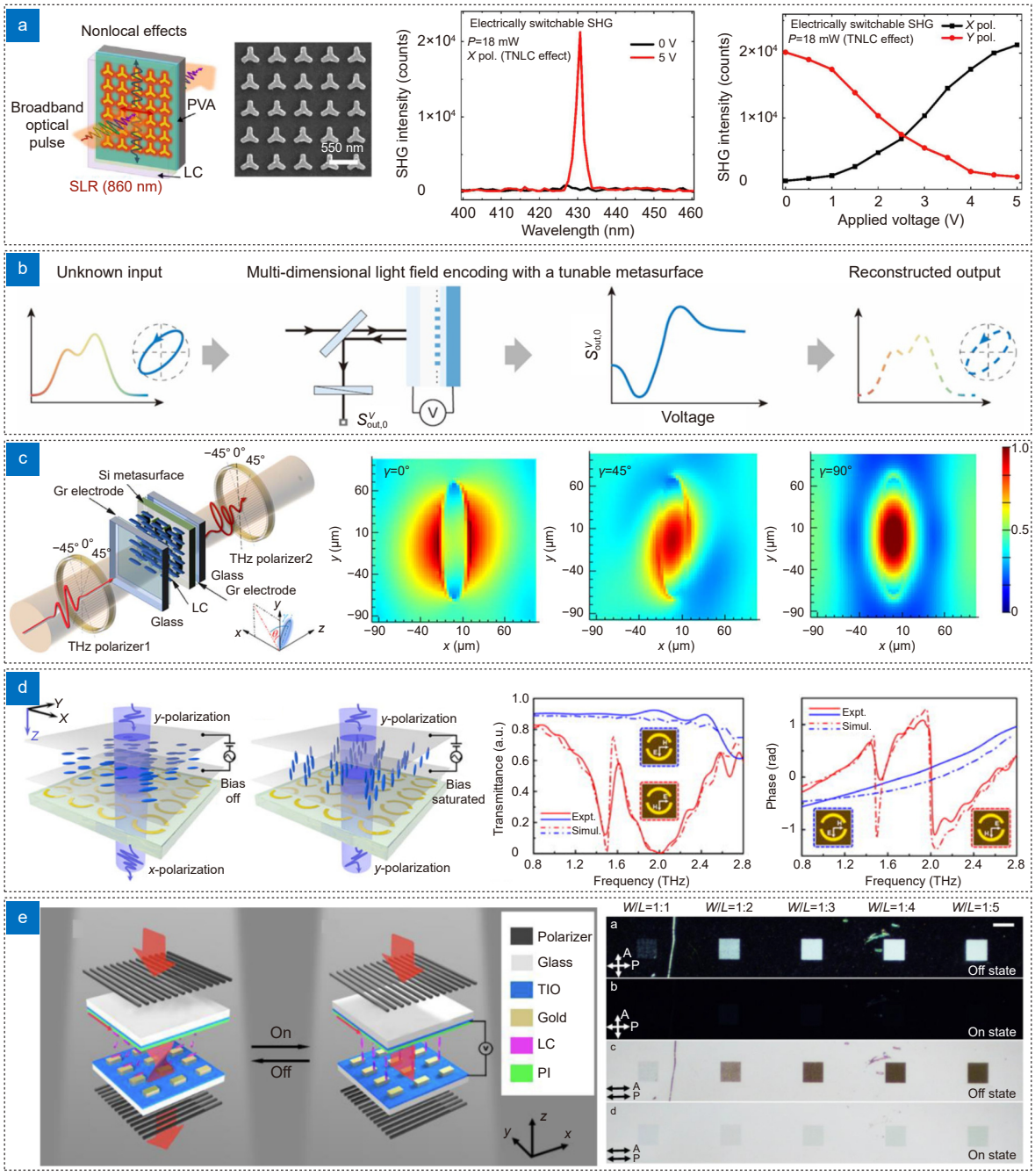

Fig. 6 | Spectral tuning in the NIR and THz region using LC-combined metasurface. (**a**) The left image depicts a schematic of the nonlinear metasurface capable of electrically tuning nonlocal second-harmonic generation by combining LC, along with a SEM image. The right image illustrates the results of electrical switching for second-harmonic generation and the second-harmonic signal. (**b**) This image shows a simplified representation of computational spectropolarimetry using a tunable LC metasurface. When light with an unknown polarization and spectrum strikes the LC metasurface, the polarization and spectrum of the incident light can be computationally reconstructed based on the measured intensity of the reflected light. (**c**) The left image shows a schematic of the proposed system for electrically tunable anisotropy and chirality. The right image shows FDTD simulations of electric field distribution at γ=0°, 45°, and 90°, where γ represents the angle between the long axis of the LC molecule orientation and the x–y plane. (**d**) The left image displays a schematic of the demonstrated active Fano resonance cloaking system. The right image presents numerical simulations, measured transmission spectra, and corresponding phase spectra for incident waves in both x-polarization (red curve) and y-polarization (blue curve). (**e**) The left image shows a schematic of the proposed tunable LC-loaded metasurfaces. The right image shows experimental results based on the ratio of width to length. Figure reproduced with permission from: (a) ref.[150], (b) ref.[151], under a Creative Commons Attribution 4.0 International License; (c) ref.[152], © 2022 Optica Publishing Group; (d) ref.[153], © 2019 AIP Publishing; (e) ref.[154], © 2021 John Wiley and Sons.

resulting in an isotropic mode with weak plasmonic resonance. In contrast, when the ratio is 1:5, isotropy increases, leading to a deeper dip in the transmissive spectra, indicating strong plasmonic resonance. Additionally, LC-based tunable polarization-dependent THz filter has been demonstrated[155].

Absorber

Absorbers, which can be employed for optical sensing/detection, optical modulators, and energy harvesting, aim to maximize energy absorption within absorbing layers. Generally, perfect absorbers require zero transmission and zero reflection (unity absorption). Realizing perfect absorbers with the use of metamaterials has garnered a lot of attention since the early times in this research field. Minimizing the transmission can usually be achieved with metallic plate at the backside. However, to minimize the reflection, the impedance mismatch should be removed, which needs control of the permeability that is challenging to achieve with natural materials but becomes feasible through the use of metamaterials[156,157]. Among the numerous studies that have attempted to realize a perfect absorber based on metasurfaces, there have been a consistent emergence of research focusing on enriching versatility by incorporating LC into these metasurface-based absorbers.

Shrekenhamer et al. first proposed a tunable metasurface absorber at THz frequencies by combining LCs[158]. The potential is applied at the electric ring resonator and ground plane, enabling the control of the permittivity of the LC layer. The frequency-dependent absorption is calculated under the different applied bias, which shows the general trend of absorption shifting to lower frequencies by increasing the voltage. Isic et al. have also demonstrated metasurface absorber which can modulate the reflectance at target frequency from nearly zero to more than 90%[159]. To achieve this, the critical coupling between periodic resonators and external fields is exploited with a careful design of resonator geometry. Consequently, this design achieves a polarization-independent tunable absorber with the ability to spectrally modulate the resonance by more than 15% with a rapid response time.

Yin et al. have proposed a tunable chiral metasurface absorber in the NIR region which has selective absorption characteristics for specific circular polarized state[160]. The metasurface absorber is composed of MIM structure consisting of two L-shaped gold nanohole arrays on the top metallic layer. LC layer is serving as the insulator layer, changing the polarization state and consequently flipped the reflecting and absorbing behaviors of chiral metasurface. It shows over 70% reflection and 80% absorption in opposite spin state, and achieves high circular dichroism reaching approximately 70%, while simultaneously flipping the sign of the circular dichroism according to the LC alignment.

LC tunable metasurface absorbers operating for dual-band have also been demonstrated at a THz region with a new resonant structure, compared to other works that can modulate only a single absorption peak[161]. The unit cell structure consists of two quartz plates encapsulating the LC layer, with a patterned layer and a ground plate made of copper printed on each side of the quartz plates. This structure excites resonance modes at the two peak absorption frequencies of 271 and 304.8 GHz at the initial LC alignment, while the rotation of LC orientation induces the redshift of the peak frequencies. This design is also insensitive to incident polarization and maintains high absorptivity at different oblique angles, which gives advantages for practical applications such as sensing and detection.

Savo et al. have demonstrated the reflective SLM at THz frequency with the metasurface absorbers integrated with LCs[162]. The proposed metasurface absorber consists of a dielectric spacer sandwiched between electric ring resonator arrays and ground plate, while the rest of the part between two gold layers is covered with LC layers. By controlling the orientation of the LC with 6 by 6-pixel array scheme, the response frequency of absorbers can be shifted, which enables modulating the spatial distribution of THz waves.

Optical platform with LC-integrated metasurface

Even the most remarkable technology faces limitations, and when these limitations are clearly defined, the scope of application becomes restricted. LCs, by introducing tunability to metasurfaces, have effectively surmounted these constraints and enhanced the flexibility of metasurfaces. This has facilitated the diverse integration of metasurfaces into various devices, including those previously mentioned, such as metaholograms, metalenses, color generation, and beam steering. In this section, we aim to present several illustrative examples.

Kim et al. have demonstrated a real-time gas-sensitive holographic device that is particularly important for

public health and environmental monitoring [Fig. 7(a)][163]. Based on the detection of gas on LCs, the polarization state of the light is changed, allowing light to pass through the metasurface only when the gas is detected. When the light passes through the metasurface, a holographic alarm is displayed to alert the user. Additionally, this group has designed a flexible metasurface using a novel nanofabrication method called nanoimprinting, which easily transfers the pattern onto a flexible substrate. Finally, this group has implemented an ultracompact gas sensor without complex systems by attaching the flexible metasurface to curved glass at a low cost. These results show that integrating LC-based metasurfaces with other components can realize promising devices.

As another example, Li et al. have implemented an encryption platform using a polarization-based LC nanoaperture metasurface [Fig. 7(b)][164]. This group designed both rectangular meta-atoms and square meta-atoms, which are dependent on and independent of polarization states, respectively. The rectangular meta-atoms exhibit plasmonic resonances only when aligned with the polarization state matching their short axis. LCs enable more possible cases because, without LCs, there are only two cases: "1 0" or "0 1" (where 0 and 1 represent off and on states, respectively, in each pixel) according to polarization direction, either 0° or 90° with respect to the short axis of rectangular meta-atoms. However, by adding LCs, there are 4 cases: "1 1", "1 0", "0 1", and "0 0" according to different polarization states and applied voltages. This concept can be used for encryption devices, and this group demonstrated this with two examples: “x” and “√” shaped marks, as well as QR code designs.

The integration of LC with a metasurface and an optical waveguide has been also demonstrated, potentially finding utility in dynamic AR displays [Fig. 7(c)][165]. Instead of vertical cascading of multiple layers of metasurfaces which presents challenges in precise alignment, total internal reflection within the optical waveguide enables successful coupling of beam steering metasurface with two different holographic metasurfaces. The beam steering metasurface in the middle of the system is designed to redirect the normally illuminated beams in opposite directions, contingent upon the *x*-/*y*- polarization of the incident light, which can be electrically controlled by integrated LC layer. Two different holographic metasurfaces on both sides of the optical waveguide can generate two different holographic images dynamically with the change of the LC voltage, which can be potentially employed for 3D stereoscopic vision[166].

In other research, improving the quality and functionality of SLMs are actively studied, which can contribute to wide range of applications such as displays, LiDAR, and optical communications. For example, a multispectral SLM has been proposed using LC-tunable FP nanocavities which enables high reflectance and 2π phase modulations at multiple wavelengths, a crucial feature for display applications[167]. The system comprises an LC layer sandwiched between two distributed Bragg reflector layers, with the thickness of each layer is carefully optimized to achieve high reflectance and large phase shifts at multiple wavelengths. The operating wavelengths are determined within the blue-shift range as the LC orientation angle transitions from 0° to 90°, allowing for full phase modulation with high reflectance. The system performance has been verified through the construction of wide FOV beam steering device and varifocal cylindrical lenses, demonstrating its significant potential for practical applications. As another example, polarization-independent SLM device is also demonstrated with 4K resolution, which is beneficial for real applications such as beam steering devices and displays[168]. Despite promising results to date, devices using LC-based metasurfaces still exhibit insufficient performance relative to their price. Therefore, we intend to conclude by summarizing several issues to be addressed.

Conclusions

In this review, we summarized several representative LC-based metasurfaces, which can dynamically modulate wavefront or spectral features. Additionally, we discussed significant research on novel optical platforms utilizing LC-based metasurfaces, such as AR/VR, encryption, and sensors. Beyond the scope covered in this review, there are still many other methods and aspects in the design and applications of photonic devices using LCs that hold potential for achieving tunability. An interesting example is LC elastomer (LCE), which has been studied as a promising candidate for realizing dynamic responses of metasurface through mechanical deformation induced by heat, light, and electricity[23]. In addition, several pieces of research related to plasmonics[169,170], chiral[171–173], and nonlinear[174,175] optics, which have been actively studied in the nanophotonic field, are also attempting to utilize LC to enrich the functionality of photonic devices. The

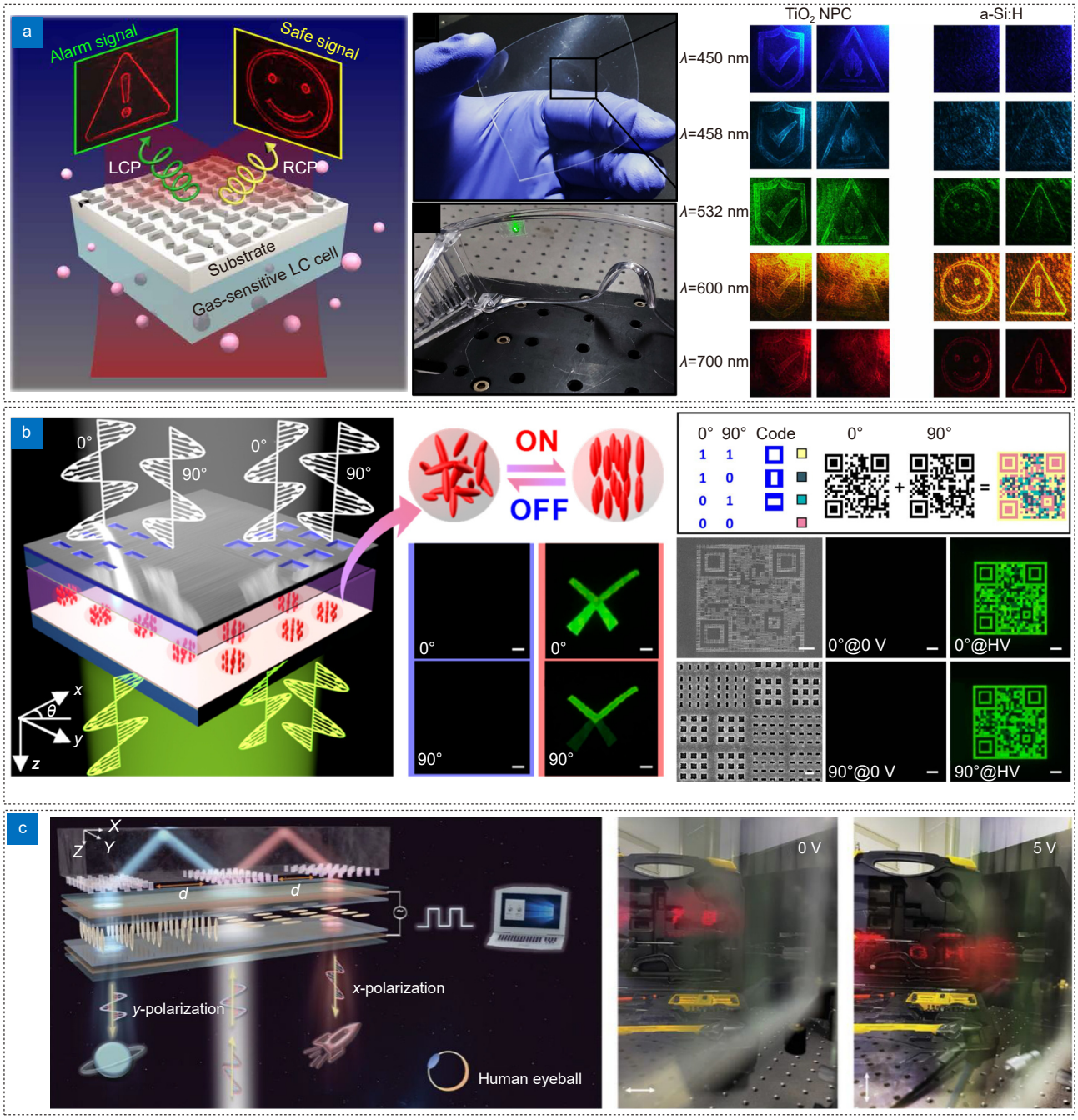

Fig. 7 | Various applications using LC-based metasurfaces. (**a**) Schematic of a gas-sensitive holographic sensor. The middle image shows proposed metasurfaces successfully combined with a curved surface. The right image demonstrates broadband properties with experimental results. (**b**) The left image illustrates a schematic of the proposed polarization-based encryption platform and possible cases based on polarization states. The right image shows the demonstrated encryption platform using this concept. (**c**) Schematic of dynamic AR system using layer-folded metasurface integrated with LC. The right image shows dynamically switchable holographic images superimposed on real-world scenes, by controlling the polarization beam with tunable LC platform. Figure reproduced with permission from: (a) ref.[163], under a Creative Commons Attribution 4.0 International License; (b) ref.[164], © 2021 American Chemical Society; (c) ref.[165], © 2022 John Wiley and Sons.

range of application area of LC-based metadevice is also extending to various unique systems, such as spectropolarimetry[151] and thermal camouflage for military use[176]. Combining LCs with these research areas can dramatically improve the performance of conventional approaches, as LCs are strong and user-friendly options for enabling versatile applications of metasurfaces.

In spite of extensive research in this field, several issues impede the versatile use of LC-based devices. One example is the fringing field effect, which indicates the

effect that electric distribution near the edges of the electrodes forms fringes and extends outside of the electrodes. This influences the adjacent pixel in the pixel-level modulating LC devices, especially when pixel pitch becomes comparably small as cell gap, thus limiting the pixel size of the modulators. It is noted that the minimum pixel size of the reflective LCoS (LC on silicon) device is about 3 μm[177,178] for 2D SLM, while researchers are striving to realize pixel pitch of 1 μm[179]. The modulation speed is also one of the critical drawbacks of LC devices. Typically, the switching speed of LC is a few milliseconds, which is comparably slower than other optical modulators. For several applications that need faster response time, LC devices with thin LC cell gap can be a general approach to resolve this issue. Additionally, in general cases, LC-based devices require pre-alignment process, usually by rubbing alignment, which can cause static electricity and mechanical damage degrading the device's performance. Especially, the alignment layer can hinder the advantage of thin LC cells, by generating dielectric shielding effect and strong anchoring effect[180]. However, there have been some research attempting to address these challenges by using metasurface, which also emphasizes the usefulness of tunable LC-integrated metasurface in this field[181,182]. Therefore, to achieve broader application of LC-based devices with the use of metasurface, further research in the fields of nanophotonics and nanofabrication is crucial, alongside the exploration of innovative ideas on device design.

Despite facing several challenges, LC-based metasurfaces facilitate the development of emerging devices with their unique features. Recently, promising future devices based on metasurfaces, such as displays, sensors, AR/VR, and LiDAR systems, have been actively studied. Furthermore, some LC-based metasurface products are beginning to be commercialized by startup companies beyond the academic field[183,184]. We believe that various brilliant design methods and advancing fabrication techniques such as inverse design[185–188], nanoimprint lithography[189–195], and 3D nanofabrication[196–200] will lead to emergence of new novel devices combined with LCs. The field of metasurfaces is expected to undergo a significant transition from scientific research to technological development, with LC-powered tunable metasurfaces playing a critical role in this process.

References

1. So S, Mun J, Park J et al. Revisiting the design strategies for metasurfaces: fundamental physics, optimization, and beyond. *Adv Mater* **35**, 2206399 (2023).
2. Yang Y, Seong J, Choi M et al. Integrated metasurfaces for re-envisioning a near-future disruptive optical platform. *Light Sci Appl* **12**, 152 (2023).
3. Yang Y, Kang H, Jung C et al. Revisiting optical material platforms for efficient linear and nonlinear dielectric metasurfaces in the ultraviolet, visible, and infrared. *ACS Photonics* **10**, 307–321 (2023).
4. Zheng GX, Mühlenbernd H, Kenney M et al. Metasurface holograms reaching 80% efficiency. *Nat Nanotechnol* **10**, 308–312 (2015).
5. Ye WM, Zeuner F, Li X et al. Spin and wavelength multiplexed nonlinear metasurface holography. *Nat Commun* **7**, 11930 (2016).
6. Wen DD, Yue FY, Li GX et al. Helicity multiplexed broadband metasurface holograms. *Nat Commun* **6**, 8241 (2015).
7. Li LL, Cui TJ, Ji W et al. Electromagnetic reprogrammable coding-metasurface holograms. *Nat Commun* **8**, 197 (2017).
8. Naeem T, Kim J, Khaliq HS et al. Dynamic chiral metasurfaces for broadband phase-gradient holographic displays. *Adv Opt Mater* **11**, 2370013 (2023).
9. Khaliq HS, Kim J, Naeem T et al. Broadband chiro-optical effects for futuristic meta-holographic displays. *Adv Opt Mater* **10**, 2201175 (2022).
10. Kim J, Oh DK, Kim H et al. Metasurface holography reaching the highest efficiency limit in the visible via one-step nanoparticle-embedded-resin printing. *Laser Photonics Rev* **16**, 2200098 (2022).
11. Ko B, Badloe T, Yang Y et al. Tunable metasurfaces via the humidity responsive swelling of single-step imprinted polyvinyl alcohol nanostructures. *Nat Commun* **13**, 6256 (2022).
12. Tseng ML, Semmlinger M, Zhang M et al. Vacuum ultraviolet nonlinear metalens. *Sci Adv* **8**, eabn5644 (2022).
13. Yang F, Lin HI, Shalaginov MY et al. Reconfigurable parfocal zoom metalens. *Adv Opt Mater* **10**, 2200721 (2022).
14. Feng WB, Zhang JC, Wu QF et al. RGB achromatic metalens doublet for digital imaging. *Nano Lett* **22**, 3969–3975 (2022).
15. Baek S, Kim J, Kim Y et al. High numerical aperture RGB achromatic metalens in the visible. *Photonics Res* **10**, B30–B39 (2022).
16. Cho H, Jeong H, Yang Y et al. Enhancement of luminous intensity emission from incoherent LED light sources within the detection angle of 10° using metalenses. *Nanomaterials* **12**, 153 (2022).
17. Ren HR, Jang J, Li CH et al. An achromatic metafiber for focusing and imaging across the entire telecommunication range. *Nat Commun* **13**, 4183 (2022).
18. Ko B, Kim J, Yang Y et al. Humidity-responsive RGB-pixels via swelling of 3D nanoimprinted polyvinyl alcohol. *Adv Sci* **10**, 2204469 (2023).
19. Gu JT, Liu Y, Meng NN et al. Structural colors based on diamond metasurface for information encryption. *Adv Opt Mater* **11**, 2202826 (2023).
20. Khaidarov E, Eschimese D, Lai KH et al. Large-scale vivid metasurface color printing using advanced 12-in. immersion photolithography. *Sci Rep* **12**, 14044 (2022).
21. Kim J, Park C, Hahn JW. Metal–semiconductor–metal metasurface for multiband infrared stealth technology using camouflage color pattern in visible range. *Adv Opt Mater* **10**, 2101930

(2022).
22. Lu JL, Sain B, Georgi P et al. A versatile metasurface enabling superwettability for self-cleaning and dynamic color response. *Adv Opt Mater* **10**, 2101781 (2022).
23. Zhuang XL, Zhang W, Wang KM et al. Active terahertz beam steering based on mechanical deformation of liquid crystal elastomer metasurface. *Light Sci Appl* **12**, 14 (2023).
24. Kim SI, Park J, Jeong BG et al. Two-dimensional beam steering with tunable metasurface in infrared regime. *Nanophotonics* **11**, 2719–2726 (2022).
25. Tao J, You Q, Li ZL et al. Mass-manufactured beam-steering metasurfaces for high-speed full-duplex optical wireless-broadcasting communications. *Adv Mater* **34**, 2106080 (2022).
26. Wang SJ, Qin WT, Zhang S et al. Nanoengineered spintronic-metasurface terahertz emitters enable beam steering and full polarization control. *Nano Lett* **22**, 10111–10119 (2022).
27. Yu NF, Capasso F. Flat optics with designer metasurfaces. *Nat Mater* **13**, 139–150 (2014).
28. Xie X, Pu MB, Jin JJ et al. Generalized pancharatnam-berry phase in rotationally symmetric meta-atoms. *Phys Rev Lett* **126**, 183902 (2021).
29. Balthasar Mueller JP, Rubin NA, Devlin RC et al. Metasurface polarization optics: independent phase control of arbitrary orthogonal states of polarization. *Phys Rev Lett* **118**, 113901 (2017).
30. Badloe T, Kim I, Kim Y et al. Electrically tunable bifocal metalens with diffraction-limited focusing and imaging at visible wavelengths. *Adv Sci* **8**, 2102646 (2021).
31. Liu XM, Zhao Q, Lan CW et al. Isotropic Mie resonance-based metamaterial perfect absorber. *Appl Phys Lett* **103**, 031910 (2013).
32. Bi K, Guo YS, Liu XM et al. Magnetically tunable Mie resonance-based dielectric metamaterials. *Sci Rep* **4**, 7001 (2014).
33. Liu CX, Rybin MV, Mao P et al. Disorder-immune photonics based on Mie-resonant dielectric metamaterials. *Phys Rev Lett* **123**, 163901 (2019).
34. Ratni B, Merzouk WA, De Lustrac A et al. Design of phase-modulated metasurfaces for beam steering in Fabry–Perot cavity antennas. *IEEE Antennas Wirel Propag Lett* **16**, 1401–1404 (2017).
35. Zhang L, Wan X, Liu S et al. Realization of low scattering for a high-gain Fabry–Perot antenna using coding metasurface. *IEEE Trans Antennas Propag* **65**, 3374–3383 (2017).
36. Anzan-Uz-Zaman M, Song K, Lee DG et al. A novel approach to Fabry–Pérot-resonance-based lens and demonstrating deep-subwavelength imaging. *Sci Rep* **10**, 10769 (2020).
37. Saba A, Tavakol MR, Karimi-Khoozani P et al. Two-dimensional edge detection by guided mode resonant metasurface. *IEEE Photonics Technol Lett* **30**, 853–856 (2018).
38. Han S, Rybin MV, Pitchappa P et al. Guided-mode resonances in all-dielectric terahertz metasurfaces. *Adv Opt Mater* **8**, 1900959 (2020).
39. Kupriianov AS, Xu Y, Sayanskiy A et al. Metasurface engineering through bound states in the continuum. *Phys Rev Appl* **12**, 014024 (2019).
40. Koshelev K, Tang YT, Li KF et al. Nonlinear metasurfaces governed by bound states in the continuum. *ACS Photonics* **6**, 1639–1644 (2019).
41. Melik-Gaykazyan E, Koshelev K, Choi JH et al. From Fano to Quasi-BIC resonances in individual dielectric nanoantennas. *Nano Lett* **21**, 1765–1771 (2021).
42. Colburn S, Zhan AL, Majumdar A. Metasurface optics for full-color computational imaging. *Sci Adv* **4**, eaar2114 (2018).
43. Lee C, Chang G, Kim J et al. Concurrent optimization of diffraction fields from binary phase mask for three-dimensional nanopatterning. *ACS Photonics* **10**, 919–927 (2023).
44. Farmani A. Three-dimensional FDTD analysis of a nanostructured plasmonic sensor in the near-infrared range. *J Opt Soc Am B* **36**, 401–407 (2019).
45. Smy TJ, Stewart SA, Rahmeier JGN et al. FDTD simulation of dispersive metasurfaces with Lorentzian surface susceptibilities. *IEEE Access* **8**, 83027–83040 (2020).
46. Jeong TI, Oh DK, Kim S et al. Deterministic nanoantenna array design for stable plasmon-enhanced harmonic generation. *Nanophotonics* **12**, 619–629 (2023).
47. Zhou M, Liu DJ, Belling SW et al. Inverse design of metasurfaces based on coupled-mode theory and adjoint optimization. *ACS Photonics* **8**, 2265–2273 (2021).
48. So S, Yang Y, Son S et al. Highly suppressed solar absorption in a daytime radiative cooler designed by genetic algorithm. *Nanophotonics* **11**, 2107–2115 (2022).
49. Lewi T, Evans HA, Butakov NA et al. Ultrawide thermo-optic tuning of PbTe meta-atoms. *Nano Lett* **17**, 3940–3945 (2017).
50. Lewi T, Butakov NA, Schuller JA. Thermal tuning capabilities of semiconductor metasurface resonators. *Nanophotonics* **8**, 331–338 (2019).
51. Malek SC, Overvig AC, Shrestha S et al. Active nonlocal metasurfaces. *Nanophotonics* **10**, 655–665 (2021).
52. Zhao XG, Schalch J, Zhang JD et al. Electromechanically tunable metasurface transmission waveplate at terahertz frequencies. *Optica* **5**, 303–310 (2018).
53. Arbabi E, Arbabi A, Kamali SM et al. MEMS-tunable dielectric metasurface lens. *Nat Commun* **9**, 812 (2018).
54. Han ZY, Colburn S, Majumdar A et al. MEMS-actuated metasurface Alvarez lens. *Microsyst Nanoeng* **6**, 79 (2020).
55. Ee HS, Agarwal R. Tunable metasurface and flat optical zoom lens on a stretchable substrate. *Nano Lett* **16**, 2818–2823 (2016).
56. Gutruf P, Zou CJ, Withayachumnankul W et al. Mechanically tunable dielectric resonator metasurfaces at visible frequencies. *ACS Nano* **10**, 133–141 (2016).
57. Malek SC, Ee HS, Agarwal R. Strain multiplexed metasurface holograms on a stretchable substrate. *Nano Lett* **17**, 3641–3645 (2017).
58. Fu XJ, Shi L, Yang J et al. Flexible terahertz beam manipulations based on liquid-crystal-integrated programmable metasurfaces. *ACS Appl Mater Interfaces* **14**, 22287–22294 (2022).
59. Zhang J, Wei XZ, Rukhlenko ID et al. Electrically tunable metasurface with independent frequency and amplitude modulations. *ACS Photonics* **7**, 265–271 (2020).
60. Zhang J, Li ZF, Shao LD et al. Dynamical absorption manipulation in a graphene-based optically transparent and flexible metasurface. *Carbon* **176**, 374–382 (2021).
61. Yao Y, Shankar R, Kats MA et al. Electrically tunable metasurface perfect absorbers for ultrathin mid-infrared optical modulators. *Nano Lett* **14**, 6526–6532 (2014).
62. Weiss A, Frydendahl C, Bar-David J et al. Tunable metasurface using thin-film lithium niobate in the telecom regime. *ACS Photonics* **9**, 605–612 (2022).
63. Shcherbakov MR, Liu S, Zubyuk VV et al. Ultrafast all-optical

tuning of direct-gap semiconductor metasurfaces. *Nat Commun* **8**, 17 (2017).
64. Isić G, Sinatkas G, Zografopoulos DC et al. Electrically tunable metal–semiconductor–metal terahertz metasurface modulators. *IEEE J Sel Top Quantum Electron* **25**, 8500108 (2019).
65. Scalari G, Maissen C, Cibella S et al. High quality factor, fully switchable terahertz superconducting metasurface. *Appl Phys Lett* **105**, 261104 (2014).
66. Ustinov AV. Experiments with tunable superconducting metamaterials. *IEEE Trans Terahertz Sci Technol* **5**, 22–26 (2015).
67. Tao H, Strikwerda AC, Fan K et al. Reconfigurable terahertz metamaterials. *Phys Rev Lett* **103**, 147401 (2009).
68. Zhu WM, Liu AQ, Zhang XM et al. Switchable magnetic metamaterials using micromachining processes. *Adv Mater* **23**, 1792–1796 (2011).
69. De Gennes PG, Prost J. *The Physics of Liquid Crystals* (Clarendon Press, Oxford, 1993).
70. Basiri A, Rafique MZE, Bai J et al. Ultrafast low-pump fluence all-optical modulation based on graphene-metal hybrid metasurfaces. *Light Sci Appl* **11**, 102 (2022).
71. Chen XQ, Zhang JF, Wen CC et al. Optical nonlinearity and non-reciprocal transmission of graphene integrated metasurface. *Carbon* **173**, 126–134 (2021).
72. Kim Y, Wu PC, Sokhoyan R et al. Phase modulation with electrically tunable vanadium dioxide phase-change metasurfaces. *Nano Lett* **19**, 3961–3968 (2019).
73. Zhang YF, Fowler C, Liang JH et al. Electrically reconfigurable non-volatile metasurface using low-loss optical phase-change material. *Nat Nanotechnol* **16**, 661–666 (2021).
74. Hui Y, Gomez-Diaz JS, Qian ZY et al. Plasmonic piezoelectric nanomechanical resonator for spectrally selective infrared sensing. *Nat Commun* **7**, 11249 (2016).
75. Cui T, Bai BF, Sun HB. Tunable metasurfaces based on active materials. *Adv Funct Mater* **29**, 1806692 (2019).
76. Tsilipakos O, Tasolamprou AC, Pitilakis A et al. Toward intelligent metasurfaces: the progress from globally tunable metasurfaces to software-defined metasurfaces with an embedded network of controllers. *Adv Opt Mater* **8**, 2000783 (2020).
77. Badloe T, Lee J, Seong J et al. Tunable metasurfaces: the path to fully active nanophotonics. *Adv Photonics Res* **2**, 2000205 (2021).
78. Abdelraouf OAM, Wang ZY, Liu HL et al. Recent advances in tunable metasurfaces: materials, design, and applications. *ACS Nano* **16**, 13339–13369 (2022).
79. Jeon N, Noh J, Jung C et al. Electrically tunable metasurfaces: from direct to indirect mechanisms. *New J Phys* **24**, 075001 (2022).
80. Ko B, Jeon N, Kim J et al. Hydrogels for active photonics. *Microsyst Nanoeng* **10**, 1 (2024).
81. Li JX, Yu P, Zhang S et al. Electrically-controlled digital metasurface device for light projection displays. *Nat Commun* **11**, 3574 (2020).
82. Fan CY, Chuang TJ, Wu KH et al. Electrically modulated varifocal metalens combined with twisted nematic liquid crystals. *Opt Express* **28**, 10609–10617 (2020).
83. Collings PJ, Patel JS. *Handbook of Liquid Crystal Research* (Oxford University Press, New York, 1997).
84. Chu F, Tian LL, Li R et al. Adaptive nematic liquid crystal lens array with resistive layer. *Liq Cryst* **47**, 563–571 (2020).
85. Dolan JA, Cai HG, Delalande L et al. Broadband liquid crystal tunable metasurfaces in the visible: liquid crystal inhomogeneities across the metasurface parameter space. *ACS Photonics* **8**, 567–575 (2021).
86. Mitov M. Cholesteric liquid crystals in living matter. *Soft Matter* **13**, 4176–4209 (2017).
87. Priestly E. *Introduction to Liquid Crystals* (Springer Science & Business Media, 2012).
88. Andrienko D. Introduction to liquid crystals. *J Mol Liq* **267**, 520–541 (2018).
89. Wu Q, Zhang HX, Jia DG et al. Recent development of tunable optical devices based on liquid. *Molecules* **27**, 8025 (2022).
90. Berreman DW. Solid surface shape and the alignment of an adjacent nematic liquid crystal. *Phys Rev Lett* **28**, 1683–1686 (1972).
91. Geary JM, Goodby JW, Kmetz AR et al. The mechanism of polymer alignment of liquid‐crystal materials. *J Appl Phys* **62**, 4100–4108 (1987).
92. Yaroshchuk O, Reznikov Y. Photoalignment of liquid crystals: basics and current trends. *J Mater Chem* **22**, 286–300 (2012).
93. Hariharan P. *Optical Holography: Principles, Techniques and Applications* 2nd ed (Cambridge University Press, Cambridge, 1996).
94. Collier R. *Optical Holography* (Elsevier, Amsterdam, 2013).
95. Blanche PA, Bablumian A, Voorakaranam R et al. Holographic three-dimensional telepresence using large-area photorefractive polymer. *Nature* **468**, 80–83 (2010).
96. He JW, Dong T, Chi BH et al. Meta-hologram for three-dimensional display in terahertz waveband. *Microelectron Eng* **220**, 111151 (2020).
97. Genevet P, Capasso F. Holographic optical metasurfaces: a review of current progress. *Rep Prog Phys* **78**, 024401 (2015).
98. Gao H, Fan XH, Xiong W et al. Recent advances in optical dynamic meta-holography. *Opto-Electron Adv* **4**, 210030–210030 (2021).
99. Yoon G, Tanaka T, Zentgraf T et al. Recent progress on metasurfaces: applications and fabrication. *J Phys D:Appl Phys* **54**, 383002 (2021).
100. Zhu SQ, Xu ZT, Zhang H et al. Liquid crystal integrated metadevice for reconfigurable hologram displays and optical encryption. *Opt Express* **29**, 9553–9564 (2021).
101. Wan CW, Li Z, Wan S et al. Electric-driven meta-optic dynamics for simultaneous near-/far-field multiplexing display. *Adv Funct Mater* **32**, 2110592 (2022).
102. Tang DL, Shao ZL, Xie X et al. Flat multifunctional liquid crystal elements through multi-dimensional information multiplexing. *Opto-Electron Adv* **6**, 220063 (2023).
103. Xie X, Du WJ, Shao ZL et al. Multichannel binary-image and holographic display based on planar liquid crystal devices. *Laser Photonics Rev* **17**, 2300193 (2023).
104. Kim I, Ansari MA, Mehmood MQ et al. Stimuli-responsive dynamic metaholographic displays with designer liquid crystal modulators. *Adv Mater* **32**, 2004664 (2020).
105. Psaltis D, Quake SR, Yang C. Developing optofluidic technology through the fusion of microfluidics and optics. *Nature* **442**, 381–386 (2006).
106. Cuennet JG, Vasdekis AE, De Sio L et al. Optofluidic modulator based on peristaltic nematogen microflows. *Nat Photon* **5**, 234–238 (2011).
107. Naveed MA, Kim J, Javed I et al. Novel spin-decoupling strate-

gy in liquid crystal-integrated metasurfaces for interactive metadisplays. *Adv Opt Mater* **10**, 2200196 (2022).
108. Kim I, Jang J, Kim G et al. Pixelated bifunctional metasurface-driven dynamic vectorial holographic color prints for photonic security platform. *Nat Commun* **12**, 3614 (2021).
109. Yang Y, Kim H, Badloe T et al. Gap-plasmon-driven spin angular momentum selection of chiral metasurfaces for intensity-tunable metaholography working at visible frequencies. *Nanophotonics* **11**, 4123–4133 (2022).
110. Asad A, Kim J, Khaliq HS et al. Spin-isolated ultraviolet-visible dynamic meta-holographic displays with liquid crystal modulators. *Nanoscale Horiz* **8**, 759–766 (2023).
111. Lee GY, Hong JY, Hwang S et al. Metasurface eyepiece for augmented reality. *Nat Commun* **9**, 4562 (2018).
112. Shi YY, Wan CW, Dai CJ et al. Augmented reality enabled by on-chip meta-holography multiplexing. *Laser Photonics Rev* **16**, 2100638 (2022).
113. Luo Y, Chu CH, Vyas S et al. Varifocal metalens for optical sectioning fluorescence microscopy. *Nano Lett* **21**, 5133–5142 (2021).
114. Wang YJ, Chen QM, Yang WH et al. High-efficiency broadband achromatic metalens for near-IR biological imaging window. *Nat Commun* **12**, 5560 (2021).
115. Afridi A, Canet-Ferrer J, Philippet L et al. Electrically driven varifocal silicon metalens. *ACS Photonics* **5**, 4497–4503 (2018).
116. Shalaginov MY, An SS, Zhang YF et al. Reconfigurable all-dielectric metalens with diffraction-limited performance. *Nat Commun* **12**, 1225 (2021).
117. Qin S, Xu N, Huang H et al. Near-infrared thermally modulated varifocal metalens based on the phase change material Sb_2S_3. *Opt Express* **29**, 7925–7934 (2021).
118. Chen WT, Zhu AY, Sanjeev V et al. A broadband achromatic metalens for focusing and imaging in the visible. *Nat Nanotechnol* **13**, 220–226 (2018).
119. Wang SM, Wu PC, Su VC et al. A broadband achromatic metalens in the visible. *Nat Nanotechnol* **13**, 227–232 (2018).
120. Zhou HP, Chen L, Shen F et al. Broadband achromatic metalens in the midinfrared range. *Phys Rev Appl* **11**, 024066 (2019).
121. Arbabi A, Arbabi E, Kamali SM et al. Miniature optical planar camera based on a wide-angle metasurface doublet corrected for monochromatic aberrations. *Nat Commun* **7**, 13682 (2016).
122. Groever B, Chen WT, Capasso F. Meta-lens doublet in the visible region. *Nano Lett* **17**, 4902–4907 (2017).
123. Engelberg J, Zhou C, Mazurski N et al. Near-IR wide-field-of-view Huygens metalens for outdoor imaging applications. *Nanophotonics* **9**, 361–370 (2020).
124. Shalaginov MY, An SS, Yang F et al. Single-element diffraction-limited fisheye metalens. *Nano Lett* **20**, 7429–7437 (2020).
125. Hu YQ, Ou XN, Zeng TB et al. Electrically tunable multifunctional polarization-dependent metasurfaces integrated with liquid crystals in the visible region. *Nano Lett* **21**, 4554–4562 (2021).
126. Jin L, Dong ZG, Mei ST et al. Noninterleaved metasurface for (2^6-1) spin- and wavelength-encoded holograms. *Nano Lett* **18**, 8016–8024 (2018).
127. Bosch M, Shcherbakov MR, Won K et al. Electrically actuated varifocal lens based on liquid-crystal-embedded dielectric metasurfaces. *Nano Lett* **21**, 3849–3856 (2021).
128. Badloe T, Kim Y, Kim J et al. Bright-field and edge-enhanced imaging using an electrically tunable dual-mode metalens. *ACS Nano* **17**, 14678–14685 (2023).
129. Wehr A, Lohr U. Airborne laser scanning—an introduction and overview. *ISPRS J Photogramm Remote Sens* **54**, 68–82 (1999).
130. Knoernschild C, Kim C, Lu FP et al. Multiplexed broadband beam steering system utilizing high speed MEMS mirrors. *Opt Express* **17**, 7233–7244 (2009).
131. Wang DK, Watkins C, Xie HK. MEMS mirrors for LiDAR: a review. *Micromachines* **11**, 456 (2020).
132. He ZQ, Gou FW, Chen R et al. Liquid crystal beam steering devices: principles, recent advances, and future developments. *Crystals* **9**, 292 (2019).
133. Komar A, Paniagua-Domínguez R, Miroshnichenko A et al. Dynamic beam switching by liquid crystal tunable dielectric metasurfaces. *ACS Photonics* **5**, 1742–1748 (2018).
134. Li SQ, Xu XW, Veetil RM et al. Phase-only transmissive spatial light modulator based on tunable dielectric metasurface. *Science* **364**, 1087–1090 (2019).
135. Chung H, Miller OD. Tunable metasurface inverse design for 80% switching efficiencies and 144° angular deflection. *ACS Photonics* **7**, 2236–2243 (2020).
136. Wu JB, Shen Z, Ge SJ et al. Liquid crystal programmable metasurface for terahertz beam steering. *Appl Phys Lett* **116**, 131104 (2020).
137. Liu CX, Yang F, Fu XJ et al. Programmable manipulations of terahertz beams by transmissive digital coding metasurfaces based on liquid crystals. *Adv Opt Mater* **9**, 2100932 (2021).
138. Neubrech F, Duan XY, Liu N. Dynamic plasmonic color generation enabled by functional materials. *Sci Adv* **6**, eabc2709 (2020).
139. Yang WH, Xiao SM, Song QH et al. All-dielectric metasurface for high-performance structural color. *Nat Commun* **11**, 1864 (2020).
140. Jang J, Badloe T, Yang Y et al. Spectral modulation through the hybridization of Mie-Scatterers and quasi-guided mode resonances: realizing full and gradients of structural color. *ACS Nano* **14**, 15317–15326 (2020).
141. Jung C, Kim SJ, Jang J et al. Disordered-nanoparticle–based etalon for ultrafast humidity-responsive colorimetric sensors and anti-counterfeiting displays. *Sci Adv* **8**, eabm8598 (2022).
142. Sun S, Yang WH, Zhang C et al. Real-time tunable colors from microfluidic reconfigurable all-dielectric metasurfaces. *ACS Nano* **12**, 2151–2159 (2018).
143. Xie ZW, Yang JH, Vashistha V et al. Liquid-crystal tunable color filters based on aluminum metasurfaces. *Opt Express* **25**, 30764–30770 (2017).
144. Lee Y, Park MK, Kim S et al. Electrical broad tuning of plasmonic color filter employing an asymmetric-lattice nanohole array of metasurface controlled by polarization rotator. *ACS Photonics* **4**, 1954–1966 (2017).
145. Driencourt L, Federspiel F, Kazazis D et al. Electrically tunable multicolored filter using birefringent plasmonic resonators and liquid crystals. *ACS Photonics* **7**, 444–453 (2020).
146. Franklin D, Frank R, Wu ST et al. Actively addressed single pixel full-colour plasmonic display. *Nat Commun* **8**, 15209 (2017).
147. Badloe T, Kim J, Kim I et al. Liquid crystal-powered Mie resonators for electrically tunable photorealistic color gradients

and dark blacks. *Light Sci Appl* **11**, 118 (2022).
148. Yang Y, Yoon G, Park S et al. Revealing structural disorder in hydrogenated amorphous silicon for a low-loss photonic platform at visible frequencies. *Adv Mater* **33**, 2005893 (2021).
149. Zou CJ, Komar A, Fasold S et al. Electrically tunable transparent displays for visible light based on dielectric metasurfaces. *ACS Photonics* **6**, 1533–1540 (2019).
150. Sharma M, Tal M, McDonnell C et al. Electrically and all-optically switchable nonlocal nonlinear metasurfaces. *Sci Adv* **9**, eadh2353 (2023).
151. Ni YB, Chen C, Wen S et al. Computational spectropolarimetry with a tunable liquid crystal metasurface. *eLight* **2**, 23 (2022).
152. Zhao HJ, Fan F, Zhang TR et al. Dynamic terahertz anisotropy and chirality enhancement in liquid-crystal anisotropic dielectric metasurfaces. *Photonics Res* **10**, 1097–1106 (2022).
153. Shen ZX, Zhou SH, Ge SJ et al. Liquid crystal enabled dynamic cloaking of terahertz Fano resonators. *Appl Phys Lett* **114**, 041106 (2019).
154. Wang JW, Li K, He HL et al. Metasurface-enabled high-resolution liquid-crystal alignment for display and modulator applications. *Laser Photonics Rev* **16**, 2100396 (2022).
155. Shih YH, Lin XY, Silalahi HM et al. Optically tunable terahertz metasurfaces using liquid crystal cells coated with photoalignment layers. *Crystals* **11**, 1100 (2021).
156. Badloe T, Mun J, Rho J. Metasurfaces-based absorption and reflection control: perfect absorbers and reflectors. *J Nanomater* **2017**, 2361042 (2017).
157. Alaee R, Albooyeh M, Rockstuhl C. Theory of metasurface based perfect absorbers. *J Phys D Appl Phys* **50**, 503002 (2017).
158. Shrekenhamer D, Chen WC, Padilla WJ. Liquid crystal tunable metamaterial absorber. *Phys Rev Lett* **110**, 177403 (2013).
159. Isić G, Vasić B, Zografopoulos DC et al. Electrically tunable critically coupled terahertz metamaterial absorber based on nematic liquid crystals. *Phys Rev Appl* **3**, 064007 (2015).
160. Yin ST, Xiao D, Liu JX et al. Reconfigurable chiral metasurface absorbers based on liquid crystals. *IEEE Photonics J* **10**, 4600909 (2018).
161. Yin ZP, Lu YJ, Xia TX et al. Electrically tunable terahertz dual-band metamaterial absorber based on a liquid crystal. *RSC Adv* **8**, 4197–4203 (2018).
162. Savo S, Shrekenhamer D, Padilla WJ. Liquid crystal metamaterial absorber spatial light modulator for THz applications. *Adv Opt Mater* **2**, 275–279 (2014).
163. Kim I, Kim WS, Kim K et al. Holographic metasurface gas sensors for instantaneous visual alarms. *Sci Adv* **7**, eabe9943 (2021).
164. Li K, Wang JW, Cai WF et al. Electrically switchable, polarization-sensitive encryption based on aluminum nanoaperture arrays integrated with polymer-dispersed liquid crystals. *Nano Lett* **21**, 7183–7190 (2021).
165. Tang J, Wan S, Shi YY et al. Dynamic augmented reality display by layer-folded metasurface via electrical-driven liquid crystal. *Adv Opt Mater* **10**, 2200418 (2022).
166. Liu ZY, Zhang C, Zhu WQ et al. Compact stereo waveguide display based on a unidirectional polarization-multiplexed metagrating in-coupler. *ACS Photonics* **8**, 1112–1119 (2021).
167. Mansha S, Moitra P, Xu XW et al. High resolution multispectral spatial light modulators based on tunable Fabry-Perot nanocavities. *Light Sci Appl* **11**, 141 (2022).
168. Zhu ZX, Wen YH, Li JQ et al. Metasurface-enabled polarization-independent LCoS spatial light modulator for 4K resolution and beyond. *Light Sci Appl* **12**, 151 (2023).
169. Kowerdziej R, Wróbel J, Kula P. Ultrafast electrical switching of nanostructured metadevice with dual-frequency liquid crystal. *Sci Rep* **9**, 20367 (2019).
170. Sharma M, Michaeli L, Haim DB et al. Liquid crystal switchable surface lattice resonances in plasmonic metasurfaces. *ACS Photonics* **9**, 2702–2712 (2022).
171. Xiao D, Liu YJ, Yin ST et al. Liquid-crystal-loaded chiral metasurfaces for reconfigurable multiband spin-selective light absorption. *Opt Express* **26**, 25305–25314 (2018).
172. Chen P, Ma LL, Hu W et al. Chirality invertible superstructure mediated active planar optics. *Nat Commun* **10**, 2518 (2019).
173. Zheng ZG, Hu HL, Zhang ZP et al. Digital photoprogramming of liquid-crystal superstructures featuring intrinsic chiral photoswitches. *Nat Photonics* **16**, 226–234 (2022).
174. Rocco D, Carletti L, Caputo R et al. Switching the second harmonic generation by a dielectric metasurface via tunable liquid crystal. *Opt Express* **28**, 12037–12046 (2020).
175. Rocco D, Zilli A, Ferraro A et al. Tunable second harmonic generation by an all-dielectric diffractive metasurface embedded in liquid crystals. *New J Phys* **24**, 045002 (2022).
176. Liu YD, Song JL, Zhao WX et al. Dynamic thermal camouflage via a liquid-crystal-based radiative metasurface. *Nanophotonics* **9**, 855–863 (2020).
177. Zhang ZC, You Z, Chu DP. Fundamentals of phase-only liquid crystal on silicon (LCOS) devices. *Light Sci Appl* **3**, e213–e213 (2014).
178. Chen HMP, Yang JP, Yen HT et al. Pursuing high quality phase-only liquid crystal on silicon (LCoS) devices. *Appl Sci* **8**, 2323 (2018).
179. Isomae Y, Shibata Y, Ishinabe T et al. Design of 1-μm-pitch liquid crystal spatial light modulators having dielectric shield wall structure for holographic display with wide field of view. *Opt Rev* **24**, 165–176 (2017).
180. Jiao MZ, Ge ZB, Song Q et al. Alignment layer effects on thin liquid crystal cells. *Appl Phys Lett* **92**, 061102 (2008).
181. Izdebskaya YV, Yang ZW, Liu MK et al. Magnetic tuning of liquid crystal dielectric metasurfaces. *Nanophotonics* **11**, 3895–3900 (2022).
182. Veetil RM, Xu XW, Dontabhaktuni J et al. Nanoantenna induced liquid crystal alignment for high performance tunable metasurface. *Nanophotonics* (2023),doi: 10.1515/nanoph-2023-0446.
183. Akselrod GM, Yang Y, Bowen P. Plasmonic surface-scattering elements and metasurfaces for optical beam steering. U. S. Patent, 10451800 (2019).
184. Akselrod GM, Yang Y, Bowen P. Tunable liquid crystal metasurfaces. U. S. Patent, 10665953 (2020).
185. So S, Mun J, Rho J. Simultaneous inverse design of materials and structures via deep learning: demonstration of dipole resonance engineering using core–shell nanoparticles. *ACS Appl Mater Interfaces* **11**, 24264–24268 (2019).
186. So S, Badloe T, Noh J et al. Deep learning enabled inverse design in nanophotonics. *Nanophotonics* **9**, 1041–1057 (2020).
187. So S, Kim J, Badloe T et al. Multicolor and 3D holography generated by inverse-designed single-cell metasurfaces. *Adv*

Mater **35**, 2208520 (2023).
188. Lee C, Lee S, Seong J et al. Inverse-designed metasurfaces for highly saturated transmissive colors. *J Opt Soc Am B* **41**, 151–158 (2024).
189. Yao YH, Liu H, Wang YF et al. Nanoimprint lithography: an enabling technology for nanophotonics. *Appl Phys A* **121**, 327–333 (2015).
190. Oh DK, Lee T, Ko B et al. Nanoimprint lithography for high-throughput fabrication of metasurfaces. *Front Optoelectron* **14**, 229–251 (2021).
191. Kang H, Lee D, Yang Y et al. Emerging low-cost, large-scale photonic platforms with soft lithography and self-assembly. *Photonics Insights* **2**, R04 (2023).
192. Seong J, Jeon Y, Yang Y et al. Cost-effective and environmentally friendly mass manufacturing of optical metasurfaces towards practical applications and commercialization. *Int J Precis Eng Manuf-Green Technol* (2023),doi:10.1007/s40684-023-00580-x.
193. Kim J, Seong J, Kim W et al. Scalable manufacturing of high-index atomic layer–polymer hybrid metasurfaces for metaphotonics in the visible. *Nat Mater* **22**, 474–481 (2023).
194. Choi H, Kim J, Kim W et al. Realization of high aspect ratio metalenses by facile nanoimprint lithography using water-soluble stamps. *PhotoniX* **4**, 18 (2023).
195. Moon SW, Kim J, Park C et al. Wafer-scale manufacturing of near-infrared metalenses. *Laser Photonics Rev* 2300929 (2024),doi: 10.1002/lpor.202300929.
196. Oran D, Rodriques SG, Gao RX et al. 3D nanofabrication by volumetric deposition and controlled shrinkage of patterned scaffolds. *Science* **362**, 1281–1285 (2018).
197. Jung W, Jung YH, Pikhitsa PV et al. Three-dimensional nanoprinting via charged aerosol jets. *Nature* **592**, 54–59 (2021).
198. Wen XW, Zhang BY, Wang WP et al. 3D-printed silica with nanoscale resolution. *Nat Mater* **20**, 1506–1511 (2021).
199. Kim WG, Kim H, Ko B et al. Freestanding, freeform metamolecule fibers tailoring artificial optical magnetism. *Small* **19**, 2303749 (2023).
200. Kim WG, Kim SJ, Lee IH et al. Nanofountain pen for writing hybrid plasmonic architectures. *Small Struct* **5**, 2300260 (2024).

Acknowledgements

This work was financially supported by the POSCO-POSTECH-RIST Convergence Research Center program funded by POSCO, the Samsung Research Funding & Incubation Center for Future Technology grant (SRFC-IT1901-52) funded by Samsung Electronics, the National Research Foundation (NRF) grants (NRF-2022M3C1A3081312, NRF-2022M3H4A1A-02074314, NRF-2022M3H4A1A02046445, NRF-2021M3H4A1A04086357, NRF-2019R1A5A8080290, RS-2024-00356928, RS-2023-00283667) funded by the Ministry of Science and ICT of the Korean government, and the Korea Evaluation Institute of Industrial Technology (KEIT) grant (No. 1415185027/20019169, Alchemist project) funded by the Ministry of Trade, Industry and Energy (MOTIE) of the Korean government. H. Kim and J. Kim acknowledge the POSTECH Alchemist fellowship, the Asan Foundation Biomedical Science fellowship, and Presidential Science fellowship funded by the MSIT of the Korean government.

Author contributions

J. Rho conceived the idea and initiated the project. D. Kang, H. Heo, and Y. Yang organized contents of liquid-crystal assisted tunable metasurfaces. D. Kang, H. Heo, and Y. Yang mainly wrote this manuscript. J. Seong, H. Kim and J. Kim were partially involved in the part of metahologram, metalens, and beam steering, respectively. All authors commented on the manuscript confirmed the submission. J. Rho guided the entire work.

Competing interests

The authors declare no competing financial interests.